



**HAL**  
open science

# Periodic Mesoporous Ionosilica Nanoparticles for Green Light Photodynamic Therapy and Photochemical Internalization of siRNA

Braham Mezghrani, Lamiaa M A Ali, Sébastien Richeter, Jean-Olivier Durand, Peter Hesemann, Nadir Bettache

► **To cite this version:**

Braham Mezghrani, Lamiaa M A Ali, Sébastien Richeter, Jean-Olivier Durand, Peter Hesemann, et al.. Periodic Mesoporous Ionosilica Nanoparticles for Green Light Photodynamic Therapy and Photochemical Internalization of siRNA. ACS Applied Materials & Interfaces, 2021, 13, pp.29325-29339. 10.1021/acsami.1c05848 . hal-03279491

**HAL Id: hal-03279491**

**<https://hal.science/hal-03279491>**

Submitted on 6 Jul 2021

**HAL** is a multi-disciplinary open access archive for the deposit and dissemination of scientific research documents, whether they are published or not. The documents may come from teaching and research institutions in France or abroad, or from public or private research centers.

L'archive ouverte pluridisciplinaire **HAL**, est destinée au dépôt et à la diffusion de documents scientifiques de niveau recherche, publiés ou non, émanant des établissements d'enseignement et de recherche français ou étrangers, des laboratoires publics ou privés.

# Periodic Mesoporous Ionosilica Nanoparticles for Green Light Photodynamic Therapy and Photochemical Internalization of siRNA.

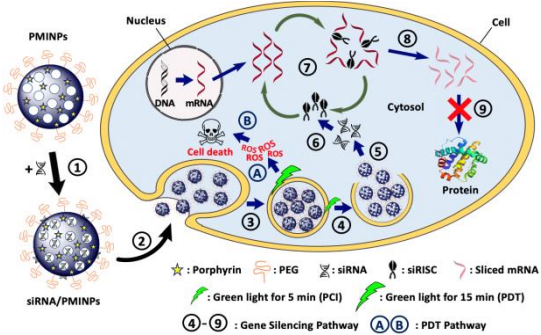
*Braham Mezghrani<sup>1,2</sup>, Lamiaa M.A. Ali<sup>1,3</sup>, Sébastien Richeter<sup>2</sup>, Jean-Olivier Durand<sup>2</sup>, Peter  
Hesemann<sup>2\*</sup> and Nadir Bettache<sup>1\*</sup>.*

<sup>1</sup> IBMM, Univ. Montpellier, CNRS, ENSCM; Avenue Charles Flahault, CEDEX 05, 34093  
Montpellier, France.

<sup>2</sup> ICGM, Univ Montpellier-CNRS-ENSCM, Montpellier, France.

<sup>3</sup> Department of Biochemistry, Medical Research Institute, University of Alexandria, Alexandria  
21561, Egypt.

# GRAPHICAL ABSTRACT



**ABSTRACT:** We report Periodic Mesoporous Ionosilica Nanoparticles (PMINPs) as versatile nano-objects for imaging, photodynamic therapy (PDT), and efficient adsorption and delivery of siRNA into breast cancer cells. In order to endow these nanoparticles PDT and siRNA photochemical internalization (PCI) properties, a porphyrin derivative was integrated into the ionosilica framework. For this purpose, we synthesized PMINPs *via* hydrolysis-cocondensation procedures from oligosilylated ammonium and porphyrin precursors. The formation of these nano-objects was attested by TEM. The formed nanoparticles were then thoroughly characterized *via* solid state NMR, nitrogen sorption, DLS, UV-Vis and fluorescence spectroscopy. Our results indicate the formation of highly porous nanorods with a length of  $108 \pm 9$  nm and a width of  $54 \pm 4$  nm. A significant PDT effect of type I mechanism ( $95 \pm 2.8\%$  of cell death) was observed upon green light irradiation in nanoparticles treated-breast cancer cells, while the blue light irradiation caused a significant phototoxic effect in non-treated cells. Furthermore, PMINPs formed stable complexes with siRNA (up to 24 h), which were efficiently internalized into the cells after 4 h of incubation mostly with energy-dependent endocytosis process. The PCI effect was obvious with green light irradiation and successfully led to  $83 \pm 1.1\%$  silencing of luciferase gene in luciferase expressing breast cancer cells, while no gene silencing effect was observed with blue light irradiation. The present work highlights the high potential of porphyrin-doped PMINPs as multifunctional nanocarriers for nucleic acids, such as siRNA, with a triple ability to perform imaging, PDT and PCI.

**KEYWORDS:** Periodic mesoporous ionosilica nanoparticles; Photodynamic therapy; siRNA; Photochemical internalization; Gene silencing.

## INTRODUCTION

Mesoporous Organosilica Nanoparticles (MON) attracted high attention in the last decade for bio-applications particularly as cancer theranostics.<sup>1-7</sup> They combine the textural features of mesoporous silica nanoparticles (MSN) with chemical function introduced by the organosilylated precursor molecules.

Mesoporous organosilica nanoparticles have been recently used in photodynamic therapy (PDT). PDT is a light-based focal therapy that makes use of the combined action of photosensitizer and light irradiation at a specific wavelength, in the presence of molecular oxygen. The high production of reactive oxygen species (ROS) as a result of PDT effect causes lipid peroxidation, protein oxidation and DNA damage, ending with cell death.<sup>8</sup>

In this context, MON containing photosensitizer molecules present excellent features for PDT applications, as their high porosity allows oxygen to diffuse in and out of the nanoparticles, combined with excellent biocompatibility.<sup>9-13</sup> In the course of our work concerning the use of Periodic Mesoporous Organosilica Nanoparticles (PMONPs) for PDT<sup>14-17</sup> and photochemical internalization (PCI) of siRNA,<sup>18-19</sup> we focus here on a new class of PMONPs, which is Periodic Mesoporous Ionosilica Nanoparticles (PMINPs). Due to their morphological and chemical polyvalence, ionosilicas appear as a particularly versatile class of periodic mesoporous organosilicas.<sup>20</sup> Ionosilica nanoparticles have recently been reported as new vectors for anionic drug delivery such as diclofenac<sup>21</sup> and theranostic applications with gemcitabine monophosphate.<sup>22</sup> These nanoparticles are synthesized from a cationic tris(triethoxysilylated) precursor, in the absence of any silica source, using sodium hexadecylsulfate as porogene that generates mesoporosity. Periodic mesoporous ionosilica nanoparticles present a high amount of

surface positive charges, a high specific surface area and ordered porosity allowing high loading of anions through anion exchange.<sup>23</sup> Due to these features, we anticipate that large anionic molecules such as nucleic acids, especially small interfering RNA (siRNA), can be loaded in or onto PMINPs. This approach appears as an interesting alternative to viral vectors, which have been used for efficient gene delivery, but which may exert immunologic and oncogenic adverse effects.<sup>24-26</sup>

The endo-lysosomal escape of nanoparticles/siRNA complex is a critical point in order to target the mRNA of interest in the cytoplasm, and it can be achieved by different possibilities such as proton sponge effect,<sup>27</sup> fusogenic groups<sup>28</sup> or photochemical internalization (PCI).<sup>29</sup>

Photochemical internalization is considered as a sub-lethal procedure since the interruption of endo-lysosomal membranes is not cytotoxic, because of the short range of action and short lifetime of the produced ROS confining the damage effect to the production site.<sup>30</sup>

Compared to PDT, PCI requires an irradiation of lower intensity in order to release siRNA molecules that have been entrapped within the endo-lysosomal compartment, so that they are not exposed to degradation and can safely reach their intended intracellular target.

In this work, we report the use of PMINPs for PDT applications, then as siRNA delivery system combined with PCI. This combination is possible due to the chemical constitution of PMINPs, containing anion exchange groups that allow efficient siRNA adsorption, together with the photodynamic properties of the immobilized porphyrin molecules. We describe the straightforward synthesis of PMINPs incorporating porphyrin molecules in the scaffold and their physico-chemical characterization. Thereafter we demonstrate the biocompatibility of the resulting functional ionosilica nanoparticles. We then report their PDT effect under green and blue light

irradiations, their ability to complex siRNA, and their gene silencing abilities promoted by the internalization of siRNA in cells through PCI. Our work highlights the high potential of PMINPs for photodynamical applications.

## RESULTS AND DISCUSSION

The synthesis of PMINPs was performed from the ammonium ionosilica precursor **1**<sup>31-32</sup> and the tetrasilylated porphyrin derivative **2**<sup>33</sup> in the molar ratio 95/5 (Figure 1). The sol gel reaction was performed in water, under basic reaction conditions, following a modified Stöber method. Sodium hexadecylsulfate (SHS) was used as a template and triethylbenzene as a swelling agent, in order to increase the pore size. The PMINPs synthesis was based on strong electrostatic interactions between the cationic organic ammonium precursor **1** and the anionic surfactant, and the simultaneous formation of covalent siloxane Si-O-Si bonds (Si-O-Si) between alkoxy silyl groups of the ionic compound **1** and the silylated porphyrin compound **2**. The addition of a non-ionic surfactant (F127) was used as an inhibitor of grain agglomeration. In order to enhance the biocompatibility of the nanoparticles, an additional surface functionalization was performed by the subsequent addition of a silylated polyethylene glycol (Silane-PEG 2000).<sup>34</sup> The successful surface modification with PEG groups was monitored via FT-IR spectroscopy (Figure S1).

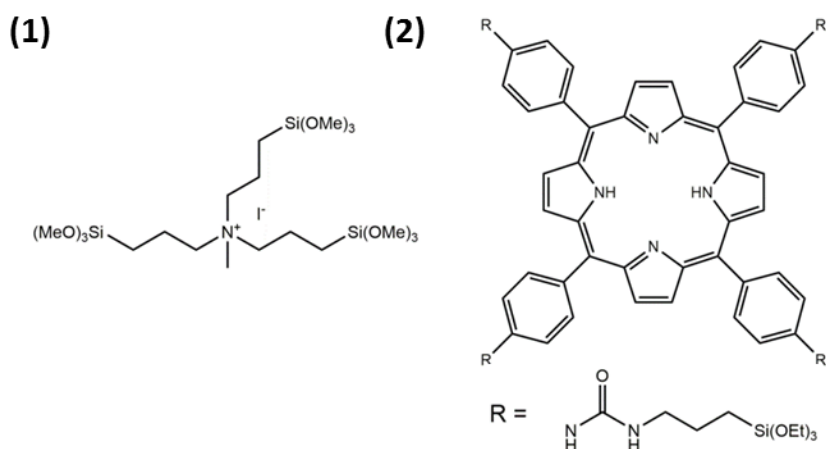


**Figure 1.** Chemical structures of nanoparticles precursors **1** and **2**.

The formation of PMINPs was attested by TEM. The obtained images (Figure 2a) reveal the presence of nanorods with  $108 \pm 9$  nm in length and  $54 \pm 4$  nm in width, displaying pore channels in a highly regular arrangement. Dynamic light scattering measurements (Figure 2b) confirm these results and indicate the formation of nanoparticles displaying monodisperse size distribution with a diameter of  $140 \pm 23$  nm,  $PDI = 0.18 \pm 0.012$ . The colloidal stability of these nanoparticles was also investigated in cell culture medium DMEM supplemented with 10% FBS using DLS. The result shows an average diameter of  $201.4 \pm 7.38$  nm and the suspension remained stable until 24 hours (data not shown). The difference observed in diameter (61.4 nm) between DLS in DMEM containing 10% FBS and DLS in water is due to the protein corona resulting of the adsorption of protein, contained in serum to the surface of nanoparticles.<sup>35-36</sup>

In order to check the chemical integrity of the ammonium and porphyrin building blocks, we performed  $^{13}\text{C}$  CP-MAS and  $^{29}\text{Si}$  CP-MAS solid-state NMR spectroscopy of the material, and the both spectra are given in Figure 2c and 2d, respectively. The  $^{13}\text{C}$  CP-MAS spectrum of the PMINPs displays large peaks at 10.9, 17.2, 49.3 and 65.0 ppm that can be attributed to the alkyl chains of the ammonium precursor, as shown by the spectrum of a material obtained from the pure ammonium precursor (Figure 2c, bottom).<sup>32</sup> It shows also additional signals at 57.9 ppm together with the large peaks in the downfield region, *i.e.*, at 118.8 and 135 ppm. These peaks indicate the presence of the porphyrin substructures in the material. Finally, the resonance at 158.2 ppm is characteristic for C=O carbon centers of urea groups. The results were confirmed *via* liquid NMR spectroscopy of the silylated porphyrin compound **2**. The  $^{13}\text{C}$  CP-MAS spectrum of the material therefore indicates the presence of both ammonium and porphyrin fragments within the nanoparticles. The  $^{29}\text{Si}$  CP-MAS spectrum of the PMINPs (Figure 2d) shows the T<sup>1</sup>, T<sup>2</sup> and T<sup>3</sup> signals at -50.4, -58.8 and -67.4 ppm, respectively. These signals can be related to silicon centers

in different chemical environments:  $T^1$  and  $T^2$  stand for silicon in  $R\underline{Si}(OSi)_1(OR)_2$  and  $R\underline{Si}(OSi)_2(OR)_1$  environments, whereas  $T^3$  represents silicon in a fully condensed  $R\underline{Si}(OSi)_3$ -environment.

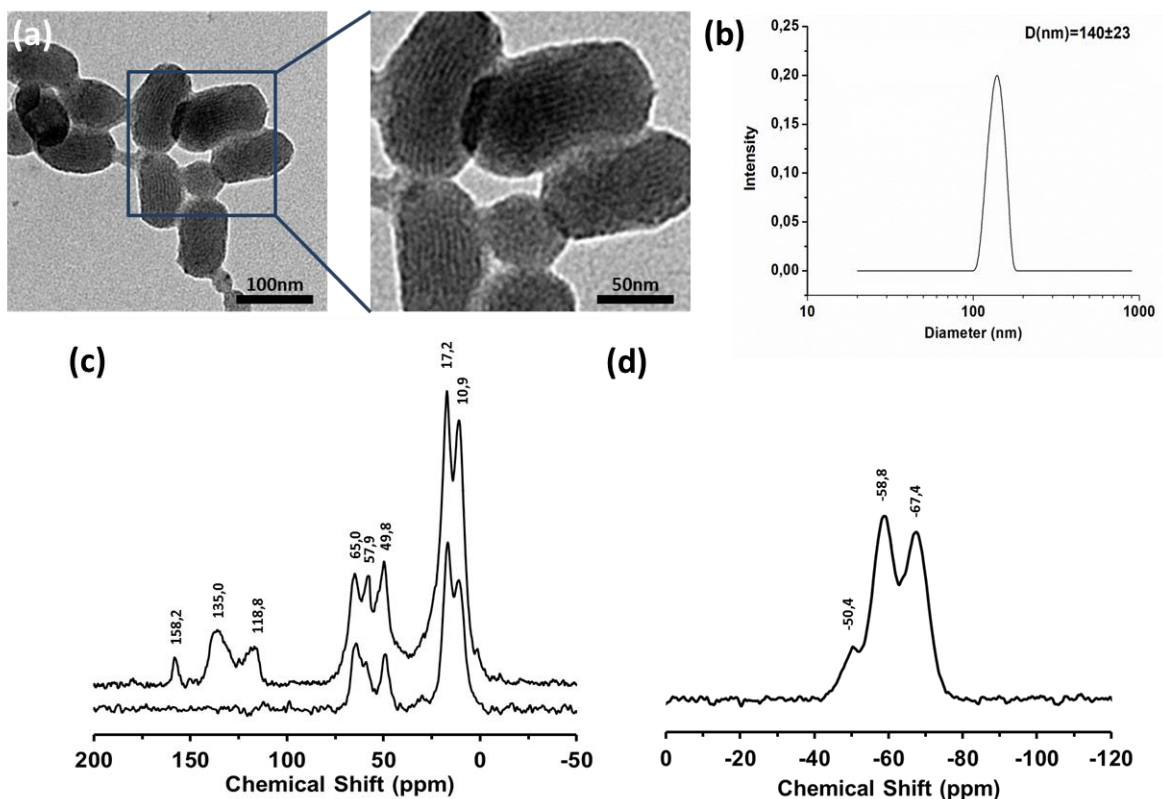


**Figure 2.** Nanoparticles' characterization. (a) TEM images of PMINPs displaying rod-shaped nanoparticles with regular pore architecture. (b) DLS measurement of PMINPs in an aqueous suspension of  $200 \mu\text{g mL}^{-1}$  at  $25^\circ\text{C}$  and  $\text{pH } 7$  ( $n = 9$ ). (c) Solid state NMR  $^{13}\text{C}$  CP-MAS of PMINPs (*top*) and a bulk ionosilica obtained from precursor **1** (*bottom*). (d)  $^{29}\text{Si}$  CP-MAS spectra of PMINPs.

The textural properties of PMINPs were studied by nitrogen adsorption experiments. The nitrogen adsorption isotherm is displayed in Figure 3a. The isotherm is of type IV and displays a

hysteresis loop between 0.4-0.6 P/P<sub>0</sub>, which is characteristic for mesoporous materials.<sup>37</sup> The nanoparticles display a specific surface area of 1015 m<sup>2</sup> g<sup>-1</sup> and a pore volume of 1.29 cm<sup>3</sup> g<sup>-1</sup>. The BJH pore size distribution was obtained from the adsorption branch of the isotherm and gives an average pore diameter of 5.1 nm (Figure 3b). This value is considerably higher compared to the formerly reported ionosilica nanoparticles,<sup>21-22</sup> due to the use of triethylbenzene as a swelling agent in the course of the hydrolysis-polycondensation reaction.<sup>31</sup> The strong increase of the isotherm at high partial pressure is due to intergrain porosity and indicates the formation of nanoparticles.

UV-Visible spectra of the precursor **2** and nanoparticles are shown in Figure 3c. The characteristic Soret absorption band of the free-base porphyrin is observed at 422 nm and the Q bands at 518, 556, 594 and 652 nm. Free base porphyrins within nanoparticles show a broad Soret absorption band at 433 nm and Q bands at 533, 573, 614 and 669 nm. The increase in absorbance of the porphyrins in the nanoparticles at lower wavelength is due to diffusion. Compared with the porphyrin precursor, absorption bands of the porphyrins within nanoparticles are red-shifted. The origin of this spectral evolution may be attributed either to the formation of porphyrin J-aggregates in the nanostructures or to the flattening of the porphyrin within the nanostructures inducing a larger  $\pi$  conjugation between the macrocycle and *meso* aryl groups.<sup>38</sup> Fluorescence spectra of the precursor **2** and nanoparticles are displayed in Figure 3d ( $\lambda_{\text{exc}} = 430$  nm). The two emission bands of porphyrins within nanoparticles at 664 and 732 nm are slightly red-shifted compared to those of the corresponding silylated porphyrin precursor (659 and 725 nm). An additional weak emission band is also observed at 611 nm when porphyrins are incorporated in the nanoparticles, likely due to the formation of aggregates.<sup>39</sup> Here, we took benefit of the emission properties of porphyrins to monitor the endocytosis of PMINPs in living cells using fluorescence microscopy.

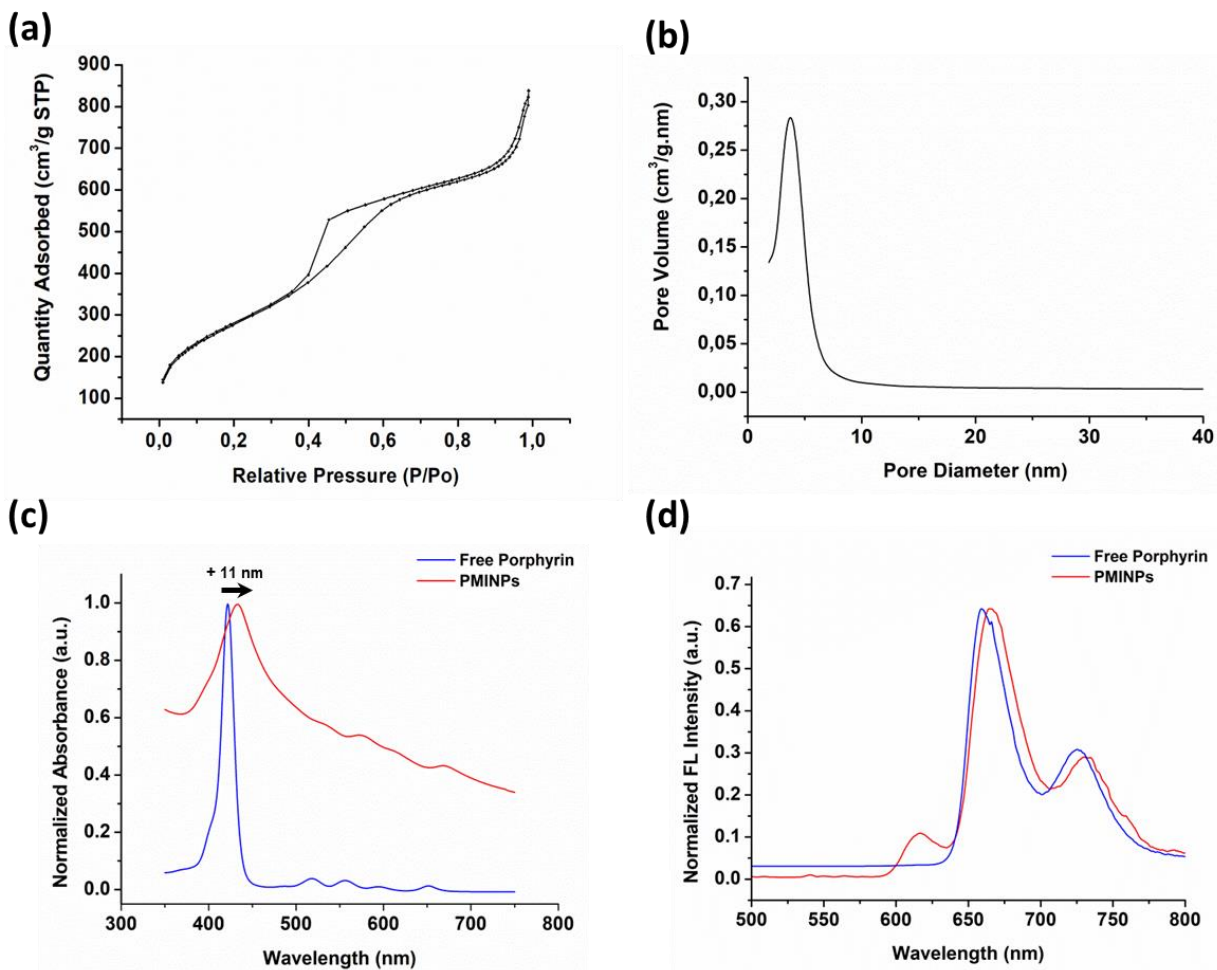


**Figure 3.** Physico-chemical characterizations of the nanoparticles. (a) Nitrogen adsorption isotherm. (b) Pore size distribution of the nanoparticles. Comparison of the (c) UV-Vis and (d) fluorescence ( $\lambda_{exc} = 430$  nm) spectra of free-porphyrin ( $100 \mu\text{g mL}^{-1}$ ) and nanoparticles ( $200 \mu\text{g mL}^{-1}$ ) in water.

After having established the formation of porphyrin-doped ionosilica nanoparticles with the incorporation of porphyrin fragments, we studied the dark toxicity and the phototoxicity of these nano-objects for siRNA adsorption, PDT and PCI applications.

The cytotoxic effect of PMINPs in the absence of light irradiation was evaluated in both breast cancer (MDA-MB-231) and healthy (HUVECs) cell lines. Cells were treated with different nanoparticle concentrations (ranging from 1 to 100  $\mu\text{g mL}^{-1}$ ) as presented in Figure 4. The cell survival was evaluated by MTT assay, which monitors the capacity of the living cells to reduce the MTT reagent to formazan crystals. The results show a similar toxic behaviour of nanoparticles in both cell lines. The cell viability values are above 70% at concentrations  $\leq 30 \mu\text{g mL}^{-1}$ , and slightly decrease to  $66 \pm 0.7\%$  and  $64 \pm 4.6\%$  for MDA-MB-231 and HUVECs, respectively, at a concentration of  $100 \mu\text{g mL}^{-1}$ . These results highlight the good biocompatibility of PMINPs<sup>21</sup> and allowed us to determine the suitable concentration range for further biological investigations.

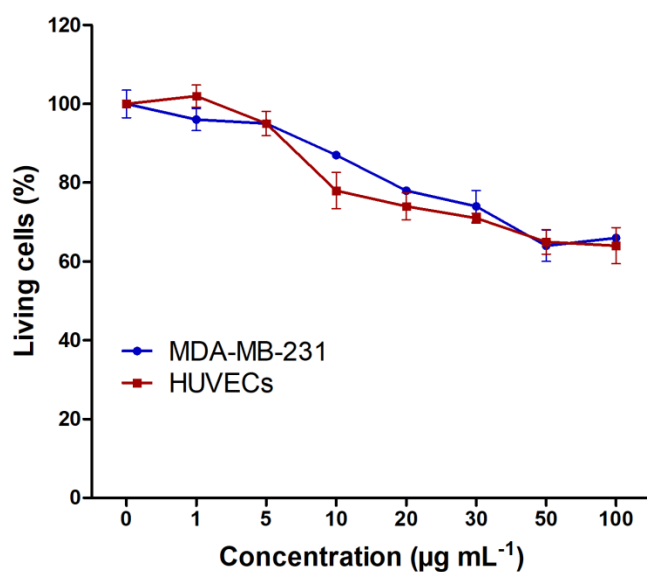


**Figure 4.** Cytotoxicity study of PMINPs on living MDA-MB-231 and HUVECs treated with different concentrations of PMINPs for 72 hours. Results are presented as mean  $\pm$  SD (n = 9).

The photodynamic efficiency of PMINPs was then studied on MDA-MB-231 cell line. Cells were treated with nanoparticles at concentrations of  $5 \mu\text{g mL}^{-1}$  and  $10 \mu\text{g mL}^{-1}$  for 24 hours, and then exposed, at a first time, to blue light irradiation (450 - 490 nm) for 15 min ( $8 \text{ J cm}^{-2}$ ), which

corresponds to the Soret absorption band of porphyrin according to the obtained UV-Vis spectrum in Figure 3c. Our results show an obvious phototoxic effect associated with the blue light irradiation of non-treated cancer cells (control), causing  $35 \pm 3.5\%$  cell death. In contrast, the treatment of the cells with  $5 \mu\text{g mL}^{-1}$  and  $10 \mu\text{g mL}^{-1}$  of PMINPs, without blue light irradiation, causes  $8 \pm 2.9\%$  and  $19 \pm 0.4\%$  of cell death, respectively, while, upon blue light irradiation condition, the cell death percentages significantly increase to  $61 \pm 2.4\%$  and  $66 \pm 1.7\%$ , respectively (Figure 5a).

In a second time, a green light irradiation at 545 nm for 15 minutes ( $34 \text{ J cm}^{-2}$ ) was applied. Compared to blue light irradiation, only  $1 \pm 0.6\%$  of cell death is observed in the irradiated control experiment, demonstrating the absence of phototoxicity with the green light. In case of absence of green light irradiation, the induced cell death values are of  $13 \pm 1.6\%$  and  $18 \pm 0.4\%$  for nanoparticle concentrations of  $5 \mu\text{g mL}^{-1}$  and  $10 \mu\text{g mL}^{-1}$ , respectively. These results are in agreement with the obtained cytotoxicity results (Figure 4). In contrast, the green light irradiation induces cell death that significantly increases to  $89 \pm 1.3\%$  and  $95 \pm 2.8\%$  for  $5 \mu\text{g mL}^{-1}$  and  $10 \mu\text{g mL}^{-1}$ , respectively (Figure 5b).

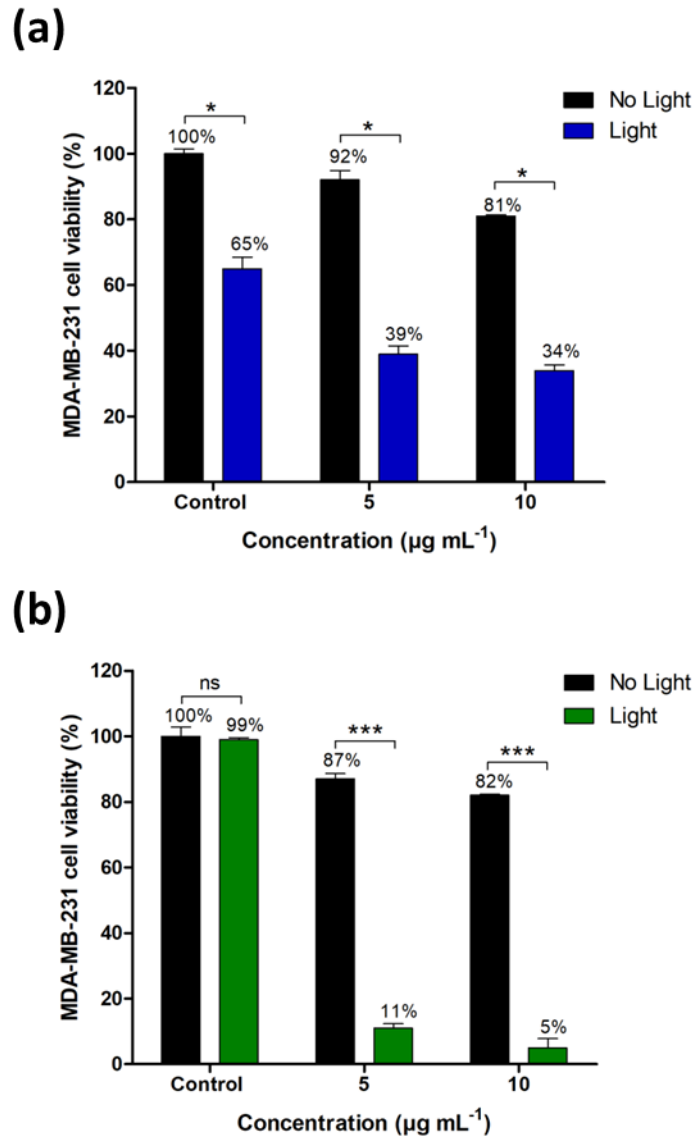


**Figure 5.** PDT effect studies of PMINPs. **(a)** PDT effect of PMINPs on MDA-MB-231 cells treated (or not) with  $5 \mu\text{g mL}^{-1}$  and  $10 \mu\text{g mL}^{-1}$  of PMINPs for 24 hours, then, either exposed (or not) to blue irradiation (450 - 490 nm) for 15 min ( $8 \text{ J cm}^{-2}$ ) or **(b)** to green light beam (545 nm) for 15 min ( $34 \text{ J cm}^{-2}$ ). The results are presented as mean  $\pm$  SD ( $n = 9$ ). \* Statistically significant difference from no light condition ( $p < 0.05$ ), \*\*\* Statistically significant difference ( $p < 0.0005$ ), ns (non statistically significant difference).

The generation of intracellular ROS is known to be a result of the photodynamic effect. The detection of ROS was carried out in MDA-MB-231 cells previously treated (or not) with PMINPs and exposed (or not) to blue light (450 - 490 nm for 15 min, 8 J cm<sup>-2</sup>) or green light (545 nm for 15 min, 34 J cm<sup>-2</sup>) irradiation using DCFDA kit assay. After cell internalization, DCFDA is transformed by ROS to a highly fluorescent derivative that can be observed by fluorescence microscopy. DCFDA mainly measures the ROS activity linked to radical hydroxyl, hydrogen peroxide and singlet oxygen.<sup>40</sup>

The obtained microscopy images were processed for the cell fluorescence intensity quantification using ImageJ software.

Our results show an absence of green fluorescence in non-irradiated control cells and non-irradiated PMINPs-treated cells as shown in Figure 6a and 6b, conditions (I) and (IV), respectively. Further, the obtained results confirm the phototoxic effect of the blue light irradiation observed on the irradiated control, shown in Figure 5a, by the visualization of green fluorescence in the cytosol of cells (Figure 6a and 6b, condition (II)), indicating ROS production. In contrast, no fluorescence is detected in the green light irradiated control (Figure 6a and 6b, condition (III)). When PMINPs-treated cells were irradiated with either blue (Figure 6a and 6b, condition (V)) or green light (Figure 6a and 6b, condition (VI)), an elevation in the cytosolic fluorescence intensity is observed, indicating an important ROS generation. Compared to blue light irradiation, these results point the safety of green light irradiation on non-treated cells and the high intracellular ROS production induced by PMINPs excitation using green light.

The difference observed between the obtained results with blue and green light irradiations prompted us to carry out further investigations.

The photo-generated formation of singlet oxygen can be monitored using the 1,3-diphenylisobenzofuran (DPBF) fluorescence quenching method. DPBF is a highly fluorescent probe that reacts with singlet oxygen forming unstable peroxide that decomposes into a non-fluorescent compound 1,2-dibenzoylbenzene, thus showing a diminution of the absorption at 410 nm.<sup>41</sup> Several suspensions of PMINPs at a concentration of 10  $\mu\text{g mL}^{-1}$  in presence of DPBF were illuminated at different irradiation times (ranging from 15 to 900 seconds) using blue light (450 - 490 nm) or green light (545 nm). In order to ensure the reliability of the results, the procedure was repeated in the same conditions using DPBF solutions in the absence of PMINPs.

The results exposed in Figure 6c show non-significant change in the absorbance values of PMINPs upon green light irradiation at any irradiation time, indicating no singlet oxygen production. The same behaviour is observed with DPBF solution alone exposed to blue or green light irradiations. Interestingly, application of blue light on PMINPs decreases gradually the absorbance values with the increase of irradiation time until 60 seconds, corresponding to the production of singlet oxygen induced by PMINPs and the decomposition of DPBF, to reach finally a steady state.

These results suggest the existence of two types of PDT mechanisms involved according to the used wavelengths. Green light irradiation generates ROS (Figure 6a and 6b), but DPBF reveals the absence of singlet oxygen (Figure 6c), thus corresponding to a PDT mechanism type (I). In contrast, blue light irradiation reveals a production of ROS and especially singlet oxygen, which corresponds to a PDT mechanism of type (II), as already described in the literature.<sup>42-43</sup>

Overall, porphyrin doped PMINPs show a clear and adjustable photodynamic effect against MDA-MB-231 cells. A comparison with other nanoparticulate systems highlight that PMINPs are among the most efficient PDT systems (table 1). These results prompted us to combine these

features with the particular anion exchange properties of the ionosilica matrix and hence to develop bifunctional nanoparticles combining PDT and siRNA carrier properties. For this reason, we focused on the delivery of siRNA promoted by PMINPs, and we studied the adsorption of siRNA with the nanoparticles more in detail.

**Table 1** Comparison of various nanoparticular PDT systems

Material	Photosensitizer	<i>in vitro</i> tumor model	wavelength	PDT efficiency (% of cell death)	ref.
Porphyrin-Ethylene-Based Periodic Mesoporous Organosilica Nanoparticles	Porphyrin	MCF-7 (human breast cancer cell line)	405 nm	80%	14
			650 nm	26%	
Zr(IV)-based porphyrinic MOF Nanoparticles	Porphyrin	HeLa (human cervical carcinoma cell line)	420 nm 630 nm	80% for both wavelengths	44
Perfluorocarbon@Porphyrin Nanoparticles	Porphyrin	HT-29 (human colorectal adenocarcinoma cell line)	650 nm	95%	45
Porphyrin-doped Magnetic Chitosan Nanoparticles	Porphyrin	SW480 (human colon adenocarcinoma cell line)	650 nm	90%	46
Porphyrin-based bridged Silsesquioxane Nanoparticles	Porphyrin	MDA-MB-231 (human breast adenocarcinoma cell line)	420 - 440 nm	44%	47
Protoporphyrin IX modified Mesoporous Silica Nanoparticles	Protoporphyrin IX	HeLa	514 nm	95%	48
Colloidal Mesoporous Silica Nanoparticles with encapsulated Protoporphyrin IX	Protoporphyrin IX	HeLa	532 nm	Cell necrosis observed by confocal microscopy 8 min after irradiation	49
Titanium Dioxide Nanoparticles conjugated with Phtalocyanine and Folic Acid	Phthalocyanine	HeLa A549 (human lung cancer cell line)	Xenon lamp 420 - 800 nm	80% 60%	50
Silica Nanoparticles conjugated with Silicon Phthalocyanine	Phthalocyanine	A375 (non pigmented human melanoma cell line)	Halogen lamp 600 - 700 nm	95%	51
Chlorin-conjugated Magnetic Nanoparticles	Chlorin e6	MGC-803 (human gastric cancer cell line)	633 nm	80%	52
Folic Acid-conjugated Graphene Oxide loaded with Chlorin	Chlorin e6	MGC-803	633 nm	90%	53
Manganese Ferrite Nanoparticle-Anchored Mesoporous Silica Nanoparticles	MnFe <sub>2</sub> O <sub>4</sub> -Chlorin e6	U-87 MG (human glioblastoma cancer cell line)	670 nm	90%	54
ZnO Nanoparticles	ZnO	SMMC-7721 (human hepatocarcinoma cell line)	254 nm	75%	55

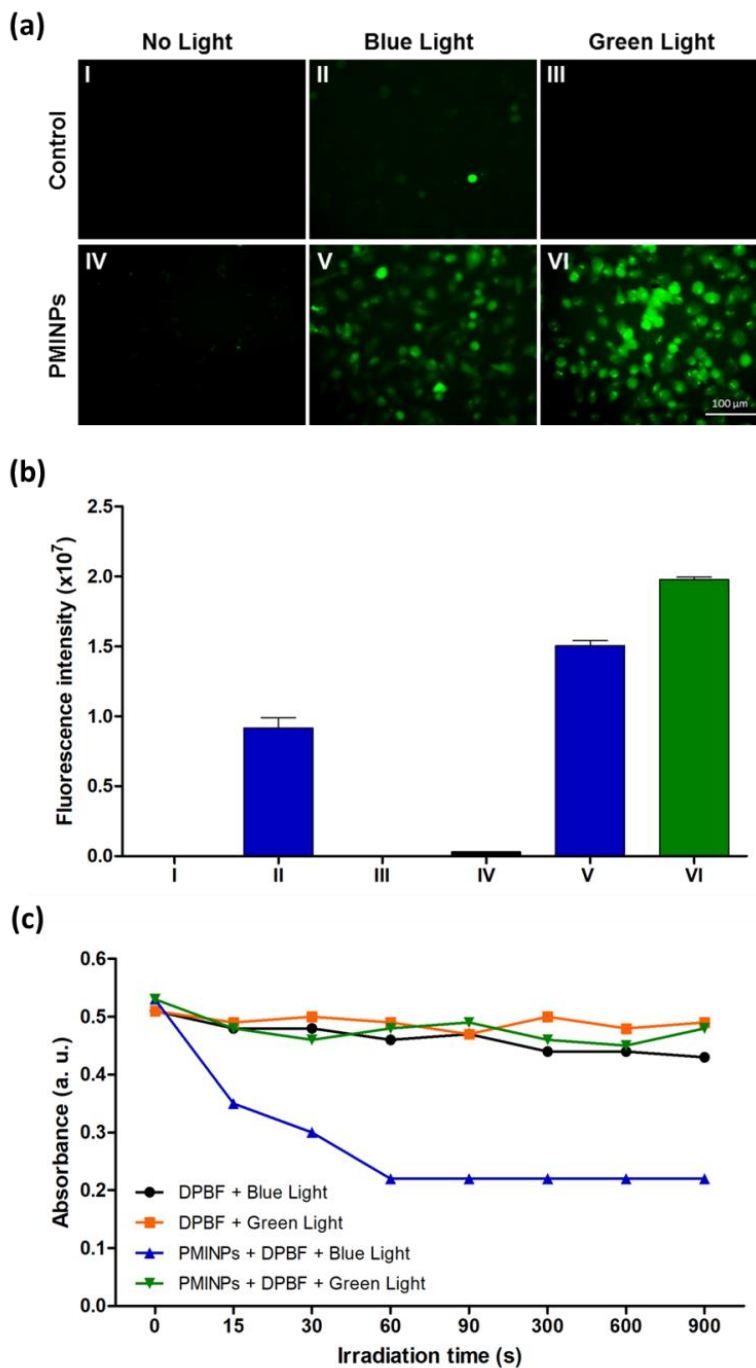


**Figure 6.** Detection of intracellular ROS and singlet oxygen generations (a) Fluorescence microscopy imaging of ROS using DCFDA assay in MDA-MB-231 cells (n = 3) treated (or not)

with  $20 \mu\text{g mL}^{-1}$  of nanoparticles for 24 h, then, exposed (or not) to blue light irradiation (15 min,  $8 \text{ J cm}^{-2}$ ) or green light irradiation (15 min,  $34 \text{ J cm}^{-2}$ ). (b) Quantification of the cell fluorescence intensity in the obtained images using ImageJ software ( $n = 6$ ). (I) Non-irradiated control, (II) Blue light irradiated control, (III) Green light irradiated control, (IV) Non-irradiated PMINPs-treated cells, (V) Blue light irradiated PMINPs-treated cells, (VI) Green light irradiated PMINPs-treated cells. (c) Detection of singlet oxygen production by the induced photo-degradation of DPBF solution mixed with or without PMINPs upon blue (450 - 490 nm) or green (545 nm) light irradiation at different irradiation times ( $n = 3$ ).

Due to the use of the ammonium precursor **1** as ionosilica precursor, PMINPs contain a large amount of positive surface charges. In order to exploit the high number of positive charges, together with the high porosity of PMINPs, nucleic acid complexation using a negatively charged siRNA was performed and monitored by agarose gel retardation assay (Figure 7a). A fixed quantity of siCtrl was added to increasing amounts of PMINPs, which led to have different siCtrl/PMINPs weight ratios, ranging from 1/3 to 1/30. Before electrophoresis, the mixture was incubated for 30 minutes at  $37^\circ\text{C}$  for the formation of siCtrl/PMINPs complexes. The analysis of the gel reveals a total retardation of siCtrl, as shown by the disappearance of siCtrl bands on the gel for all the weight ratios. Even at low weight ratio (1/3), where siRNA represents 33% (w/w), no free siRNA can be detected.

Then, the stability of the siRNA/PMINPs complex was studied, in order to verify if there was an eventual release of siRNA from the complex over time (Figure 7b). A fixed quantity of siCtrl was added to an amount of PMINPs, in a way to respect a weight ratio of 1/10. The complexes were left at  $37^\circ\text{C}$  for different time intervals from 30 minutes to 24 hours. After that, all samples

were electrophorized on agarose gel. Gel analysis results show no detection of free siCtrl bands at all tested time points, confirming the absence of any released siRNA even until 24 hours.

These results reflect the high affinity and binding capacity of PMINPs for siRNA, and also the high stability of the siRNA/PMINPs complex.

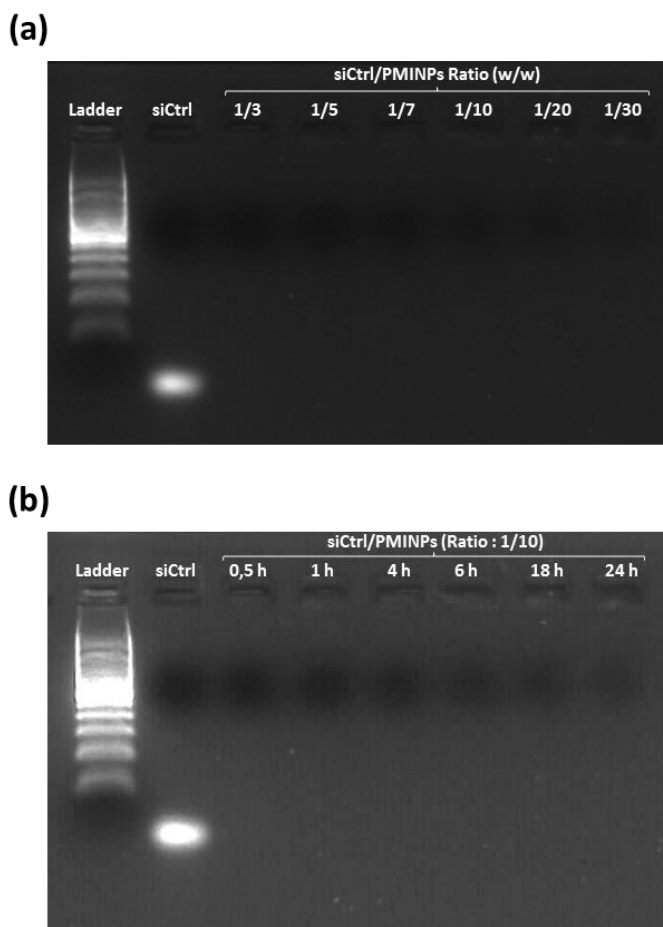


**Figure 7.** siRNA complexation studies. (a) Agarose gel retardation assay for nanoparticles complexed with siCtrl at different weight ratios ranging from 1/3 to 1/30. Electrophoresis was immediately performed after complex formation for 30 min at 37°C. (b) Stability study of the siCtrl/PMINPs complex at the weight ratio 1/10 using agarose gel retardation assay. Before electrophoresis, the complexes were formed for 30 min, 1 h, 4 h, 6 h, 18 h and 24 h at 37°C.

In a second series of experiments, we used zeta potential measurements to monitor the variation of the surface charge of the nanoparticles induced by siRNA adsorption. Due to the high number of positive surface charges, free PMINPs display a positive zeta potential of +35.8 mV (Figure 8a). After siRNA adsorption at different siRNA/PMINPs weight ratios (from 1/10 to 1/60 w/w), this value progressively decreases to +10.2 mV, -15.5 mV, -27.6 mV, to reach a plateau around -30 mV for the increasing surface coverages, thus assuming that the whole surface of the PMINPs is covered by siRNA at the lowest used PMINP amounts.

Similarly, DLS measurements were performed with free PMINPs and on complexes with a fixed weight ratio (1/10), using different siCtrl/PMINPs combinations: 50, 100 and 200 nM siCtrl with 7, 14 and 28  $\mu\text{g mL}^{-1}$  of PMINPs, respectively (Figure 8b). DLS results indicate that the diameter of the nanoparticles increases after siRNA complexation, from  $140 \pm 23$  nm for undecorated PMINPs, to around 300 nm after siRNA complexation. More specifically, we observed a clear trend regarding the size of the siRNA/PMINPs complexes as a function of the applied quantity of siRNA (in nM), with particle size of  $290 \pm 37$  nm for 50 nM,  $320 \pm 41$  nm for 100 nM and  $349 \pm 55$  nm for 200 nM siRNA.

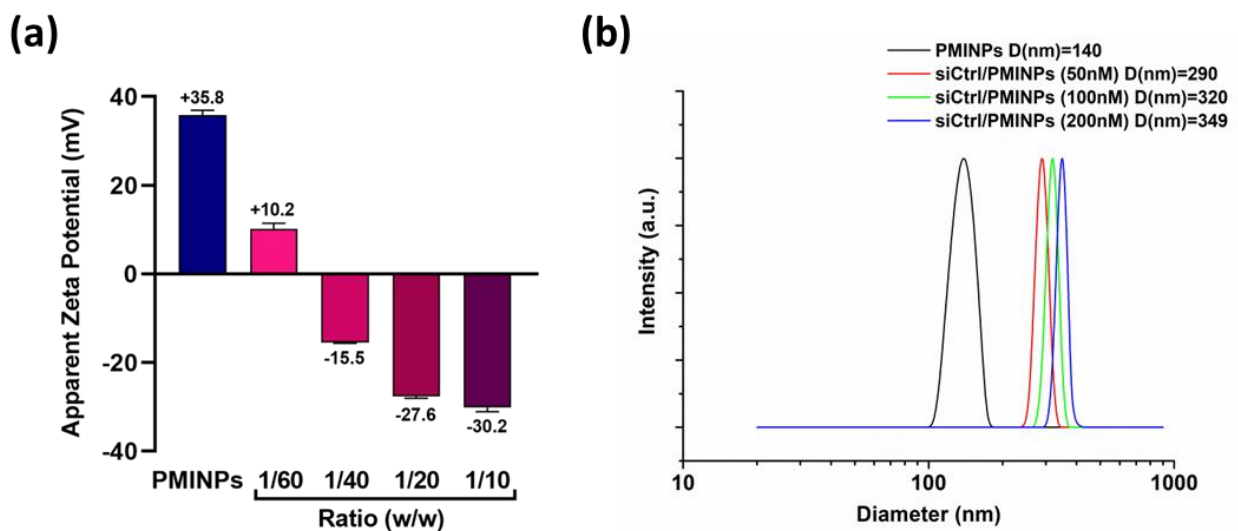


**Figure 8.** siCtrl/PMINPs complex characterization. (a) Zeta potential measurements of free-PMINPs ( $200 \mu\text{g mL}^{-1}$ ) and siCtrl/PMINPs complexes using increasing weight ratios from 1/10 to 1/60 ( $n = 3$ ). (b) DLS measurements of free-PMINPs compared to siCtrl/PMINPs complexes using increasing amounts of siCtrl from 50 to 200 nM at a weight ratio of 1/10 ( $n = 3$ ).

All these results give a clear evidence of the complexation of siRNA by PMINPs. The adsorption of the siRNA mainly occurs on the surface of the nanoparticles, as shown by a diminution in zeta potential and an elevation in the size of the nanoparticles after complexation.

In the following, we focused, in particular, on cellular uptake of the siRNA/PMINPs complexes and the induced biological activity of the internalized siRNA. For this purpose, we selected siRNA/PMINPs complexes formed at a ratio of 1/10 (w/w), which ensures good biocompatibility. Since siRNA complexation by PMINPs was successfully demonstrated, the kinetics of cell internalization of the siRNA/PMINPs complexes was studied in MDA-MB-231 cells and compared to PMINPs alone, using fluorescence intensity measurements. The cells were treated

with PMINPs or with siCtrl-ATTO-488/PMINPs at a weight ratio of 1/10 at various time points and incubated at 37°C. Our results demonstrate that the internalization rates of both PMINPs and siCtrl/PMINPs complex gradually increase to reach almost similar values of  $16.5 \pm 1.7\%$  and  $17.9 \pm 0.2\%$  respectively, after 4 h of treatment, then become stable reaching values of  $16.6 \pm 0.6\%$  for PMINPs and  $18.4 \pm 1.3\%$  for the complex siCtrl/PMINPs after 24 h (figure 9). From this result, we can conclude that the time of incubation of 4 h is sufficient to reach the maximum capability of cells to internalize both bare nanoparticles and siCtrl/PMINPs complexes.

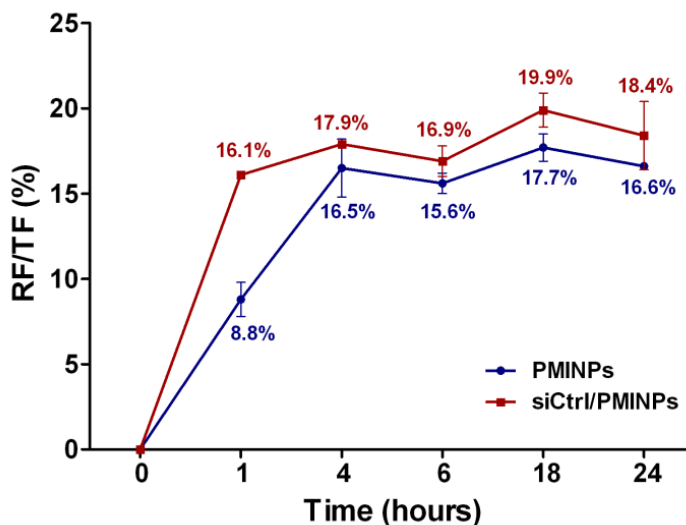


**Figure 9.** Uptake kinetic study using fluorescence intensity measurements in living MDA-MB-231 cells treated with PMINPs and siCtrl-ATTO-488/PMINPs complex at 37°C at different time intervals. Results are presented as mean  $\pm$  SD (n = 9).

The cellular uptakes of PMINPs and siRNA/PMINPs complexes were also qualitatively evaluated in MDA-MB-231 cells after 4 h of the treatment using confocal microscopy. The microscopy images shown in Figure 10 reveal that free PMINPs are endocytosed inside the cells

(green staining) and, moreover, in case of complexation, PMINPs are able to deliver the siCtrl-ATTO-488 into the cytosol (white staining) as compared with Lipofectamine. In contrast, the free siCtrl-ATTO-488 does not penetrate cells since a weak fluorescence of siCtrl-ATTO-488 is observed around the cell membranes in only few cells. This result provides an evidence of the efficient siRNA transfection inside MDA-MB-231 cells by PMINPs.

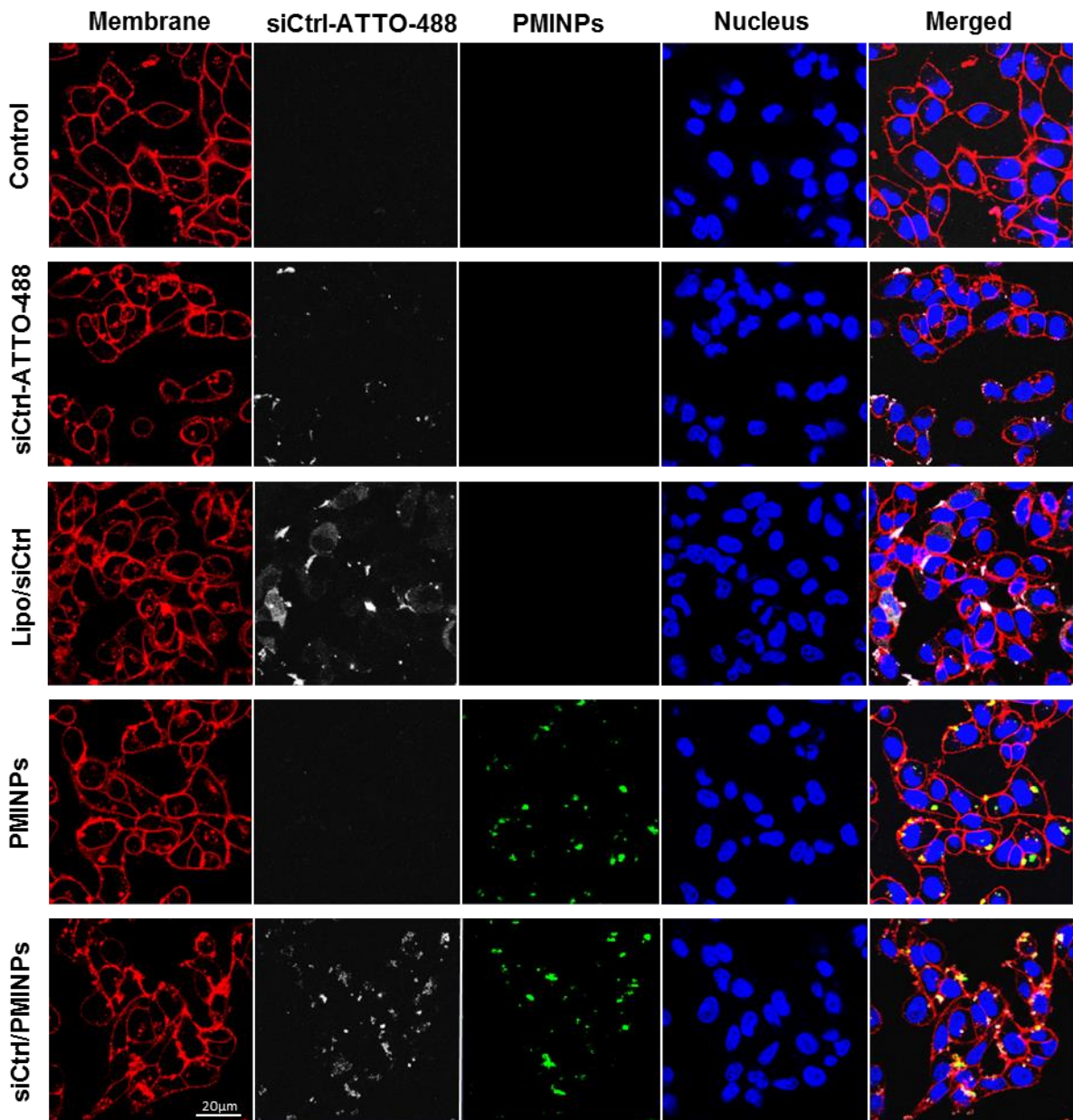


**Figure 10.** Confocal microscopy images of living MDA-MB-231 breast cancer cells untreated or treated with free siCtrl-ATTO-488, lipofectamine/siCtrl-ATTO-488, free-PMINPs and siCtrl-ATTO-488/PMINPs complex at 1/10 weight ratio (n = 3). Cell membrane, siCtrl, PMINPs, and nucleus appear in red, white, green and blue colors, respectively.

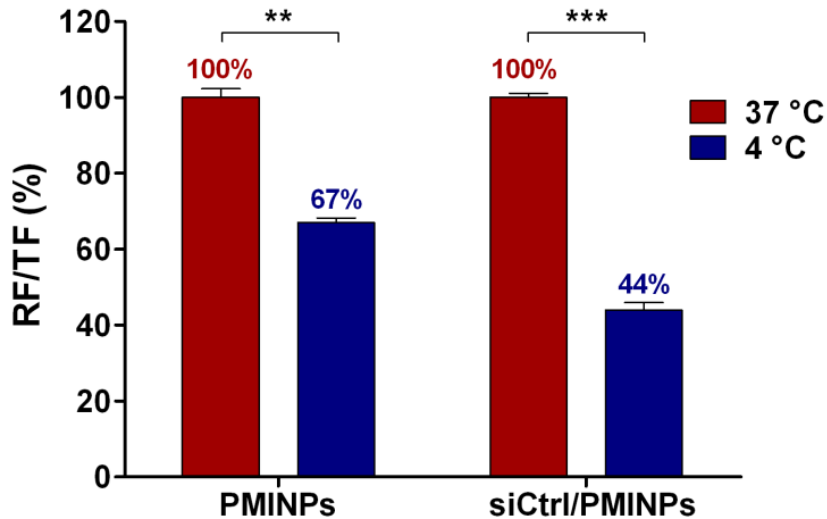


**Figure 11.** Effect of temperature on the cellular uptake of MDA-MB-231 cells incubated with PMINPs and siCtrl-ATTO-488/ PMINPs for 4 h at 4°C and 37°C using fluorescence intensity measurements. Results are presented as mean  $\pm$  SD (n = 9). \*\* Statistically significant difference from cellular uptake at 37 °C ( $p < 0.005$ ), \*\*\* Statistically significant difference ( $p < 0.0005$ ).

After having evaluated the cell internalization of the complex siRNA/PMINPs and the free carrier PMINPs, we investigated their cellular uptake pathways. For this reason, MDA-MB-231 cells were treated with PMINPs or siCtrl-ATTO-488/PMINPs using cold medium and left for 4 h at 4°C. The same procedure was repeated but this time, the cells were allowed to grow normally at 37°C, and the cell internalization rates were monitored by fluorescence intensity measurements for the both conditions (Figure 11). Indeed, the exposure of cells to low temperature (4°C) is a

commonly used method for non-specific inhibition of endocytosis.<sup>56-57</sup> Lowering the temperature from 37 to 4°C inhibits significantly the uptake of PMINPs and siCtrl/PMINPs by  $33 \pm 1.1\%$  and  $56 \pm 1.9\%$  respectively, indicating that the uptake is temperature-dependent. This result suggests that an energy-dependent endocytosis process can be the responsible for the uptake of 56% of the internalized complexes while the remaining 44% may be attributed to physical adhesion or direct translocation.

Finally, we studied the biological activity of the internalized siRNA/PMINPs complexes, using siRNA targeted against the luciferase gene, in MDA-MB-231-Luc-RFP cell line, and compared it with Lipofectamine™RNAiMAX used as a positive control of transfection. In the presence of luciferase, luciferin is oxidized into oxyluciferin with generation of luminescence. If siFluc is efficiently delivered, the formation of luciferase should be inhibited, resulting in a decrease in the luminescence. Figure 12a shows that free siFluc does not significantly decrease the luciferase expression when incubated with cells (purple bar) as only  $6 \pm 2.8\%$  of luciferase activity is inhibited. This result is in agreement with the confocal microscopy imaging results displayed in Figure 10, which confirms the inability of free siRNA to penetrate into the cells.<sup>58</sup> Free-PMINPs with green light irradiation at 545 nm for 5 minutes ( $11.3 \text{ J cm}^{-2}$ ) do not induce a luminescence decrease, proving that at 5 minutes irradiation, the phototoxicity of PMINPs has no impact on luciferase activity (Figure 12a, black bars). Furthermore, when siFluc is complexed with PMINPs at weight ratio 1/10 using different concentrations and incubated with MDA-MB-231-Luc-RFP cells without light irradiation, the luminescence values are not significantly decreased, with only  $4 \pm 2.4\%$ ,  $13 \pm 2.6\%$  and  $17 \pm 0.9\%$  for 50, 100 and 200 nM siFluc, respectively (Figure 12a, red bars). In contrast, when siFluc/PMINPs complexes were irradiated at 545 nm and for 5 minutes ( $11.3 \text{ J cm}^{-2}$ ) after eight hours of cells treatment, the complex efficiently inhibits the luciferase

activity in a dose-dependent manner (Figure 12a, green bars), values are  $60 \pm 0.8\%$  and  $62 \pm 1.1\%$  for 50 and 100 nM siFluc concentrations, respectively. Interestingly, the complex siFluc/PMINPs at a siFluc concentration of 200 nM has a more significant effect on luciferase activity than the positive control lipofectamine/siFluc (Figure 12a, pink bar), the inhibition rates are  $83 \pm 1.1\%$  and  $55 \pm 2.2\%$  for siFluc/PMINPs and lipofectamine/siFluc, respectively. The MTT assay was carried out to take into account only the luciferase expression by living cells.

The same experiment using siFluc/PMINPs complexes was repeated upon blue light irradiation (450 - 490 nm) for 5 min ( $2.6 \text{ J cm}^{-2}$ ). The results presented in Figure 12b reveal the absence of any effect on luciferase activity.

The obtained results demonstrate the strong gene silencing potential of siRNA/PMINPs complexes upon green light irradiation. This activity is probably due to a photochemical internalization mechanism,<sup>59</sup> which disrupts the endosome-lysosome membranes and releases the siRNA into the cytosol of cells.

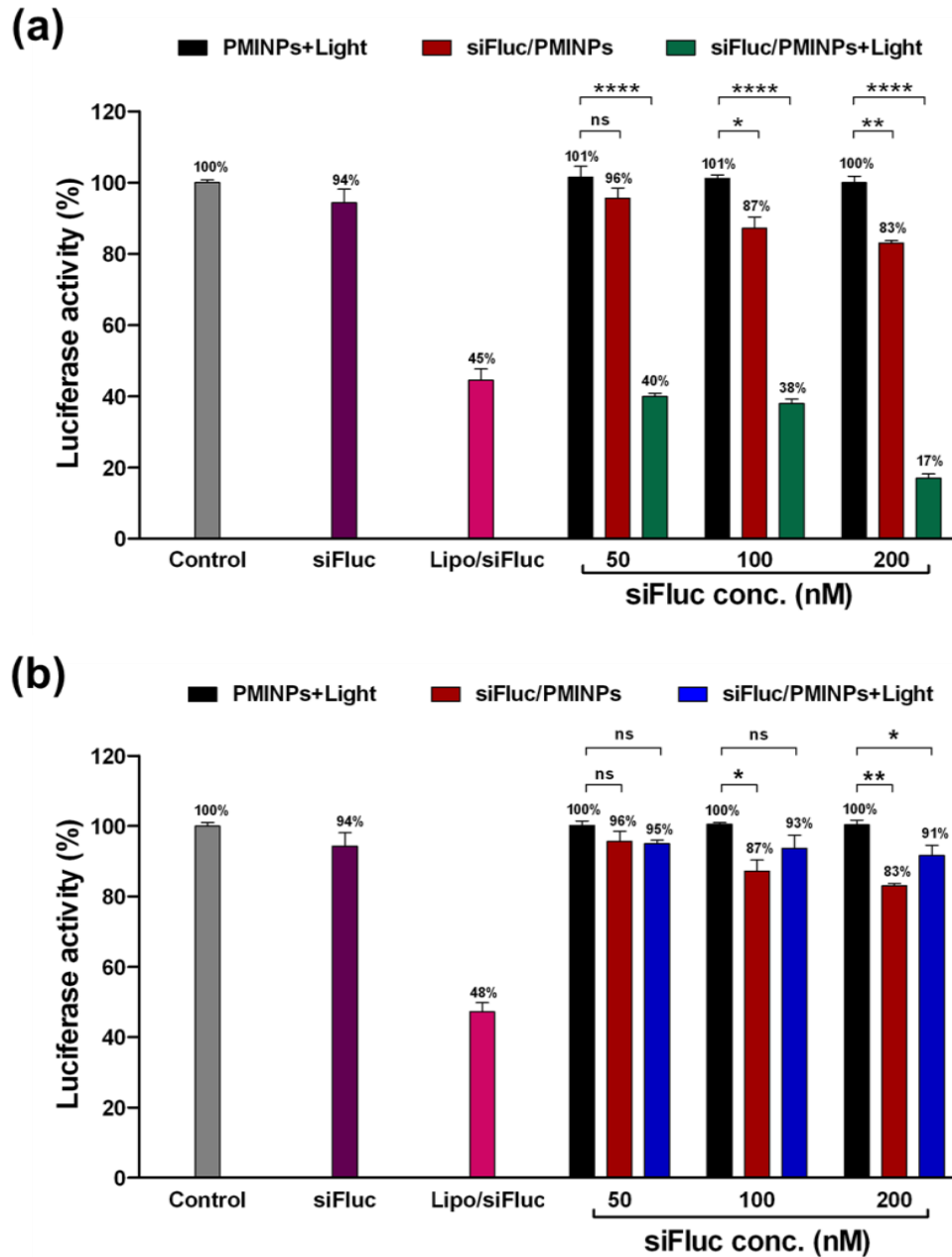


**Figure 12.** Evaluation of the biological activity and the PCI effect of the internalized siFluc/PMINPs complexes in MDA-MB-231 cells expressing luciferase and exposed (or not) to green light irradiation (a) or blue light irradiation (b) by the measurement of luminescence related to luciferase activity. Grey bar, purple bar and pink bar represent untreated cells (control), cells treated with free-siFluc (100 nM) and cells treated with lipofectamine/siFluc, respectively. Black

bars represent treated cells with different concentrations (7, 14 and 28  $\mu\text{g mL}^{-1}$ ) of free nanoparticles and irradiated with green light irradiation (545 nm, for 5 min, 11.3  $\text{J cm}^{-2}$ ) (a) or blue light irradiation (b) (450 - 490 nm, for 5 min, 2.6  $\text{J cm}^{-2}$ ) after 8 hours of incubation. Red bars represent cells treated with siFluc/PMINPs complexes (50, 100 and 200 nM siFluc mixed in 1/10 weight ratio with 7, 14 and 28  $\mu\text{g mL}^{-1}$  PMINPs, respectively) and not exposed to irradiation. Green and blue bars represent the former treatment accompanied by green light irradiation or blue light irradiation, respectively after 8 hours of incubation. For both conditions, luciferase activity was measured after 48 h of treatment and cell viability was estimated by MTT assay to consider only luciferase expression by living cells. The results are presented as mean  $\pm$  SD (n = 9), ns is non-statistically significant, \* and \*\* Statistically significant difference ( $p < 0.05$  and  $p < 0.005$  respectively), \*\*\*\* Statistically significant difference ( $p < 0.0001$ ).

In order to prove the existence of the PCI mechanism, confocal microscopy was used to verify the cellular uptake of siRNA/PMINPs complexes, their subcellular localization and the cytosolic delivery of siRNA, in the absence or in the presence of green light irradiation. As shown in Figure 13, the siCtrl/PMINPs complexes (green staining) are taken up in MDA-MB-231 cells and localized in granular vesicles representing the endo-lysosomal compartments (red staining), in the absence of green light irradiation. The yellow stain in the merged image (mentioned with arrows) is generated as a result of green (siCtrl/PMINPs) and red (endo-lysosomal compartments) fluorescence overlapping, indicating a co-localization and an accumulation of the complexes in endocytic vesicles. Two hours post light treatment, a diffused red fluorescence (pointed with circles) and a reduction of the punctuated fluorescence pattern are observed, demonstrating the disruption of the endo-lysosomal membranes suggested by PCI mechanism and the release of

siCtrl/PMINPs complexes and/or siCtrl molecules from the endo-lysosomes into the cytosol. Few yellow dots are also observed indicating an ongoing photochemical process. These results indicate the efficiency of the PCI mechanism for the endo-lysosomal liberation of siRNA, triggered by green light and delivered by PMINPs carriers.

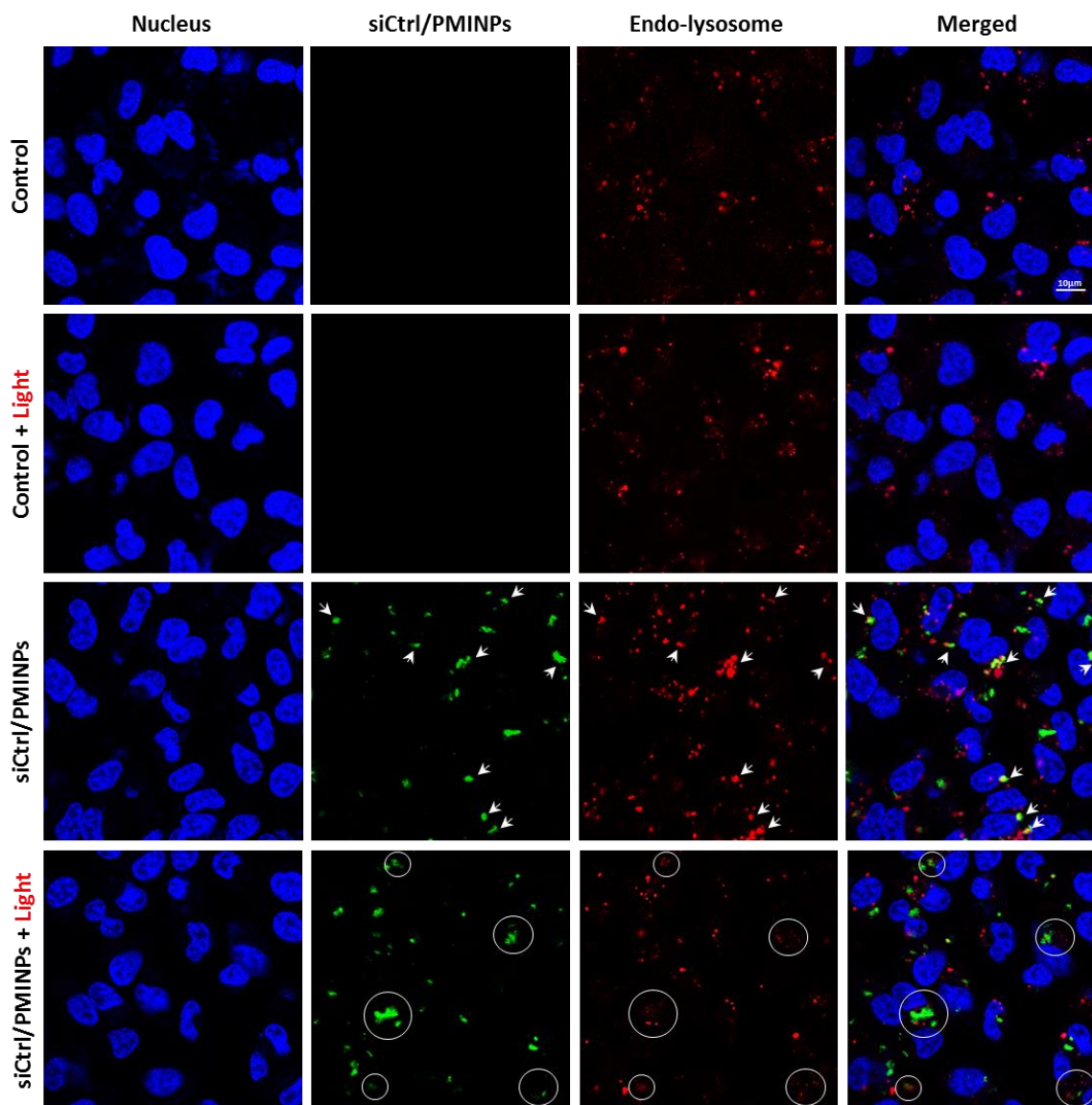


**Figure 13.** Confocal microscopy images of living MDA-MB-231 cells untreated or treated with siCtrl/PMINPs complexes for eight hours and exposed or not to green light irradiation for 5 min at 545 nm ( $11.3 \text{ J cm}^{-2}$ ) ( $n = 3$ ). Nucleus, siCtrl/PMINPs and lysosome appear in blue, green and

red color, respectively. In the case of siCtrl/PMINP treated cells, the punctuated pattern in absence of light indicates the co-localization (yellow color) of endocytic vesicles with siCtrl/PMINPs is shown in merged image (arrows). After light irradiation, a diffuse pattern (circles) is observed, where the fluorescence is spread throughout the cytosol of cells, as a result of photo-induced disruption of the endo-lysosomal membranes. Scale bar is 10  $\mu$ m.

## CONCLUSION

In this work, we have successfully performed the synthesis of biocompatible nanoparticles using an ammonium ionosilica precursor and a porphyrin derivative. PMINPs have demonstrated their ability as multifunctional theranostic nano-tools: (i) The presence of porphyrin in the scaffold endowed our model the ability of imaging and PDT thanks to its fluorescence properties and production of intracellular ROS after green light irradiation; and (ii) The high number of positive surface charges allowed an efficient siRNA complexation and subsequent siRNA delivery into the cytoplasm of cells *via* PCI mechanism triggered by green light irradiation, which resulted in an effective luciferase gene silencing. Altogether, the results obtained with the PMINPs, such as imaging, PDT and gene silencing, are promising to pursue our investigations for the use of PMINPs as efficient nano-devices for theranostic purposes.

## EXPERIMENTAL SECTION

### Materials

(3-Aminopropyl) trimethoxysilane, (3-chloropropyl) trimethoxysilane, *N,N'*-diisopropylethylamine, sodium hexadecyl sulfate (containing 40% sodium stearyl sulfate) and anhydrous 1-propanol were purchased from abcr GmbH, Germany. Iodomethane, 3-(triethoxysilyl) propyl isocyanate, 1,3,5-triethylbenzene, 1,3-diphenylisobenzofuran, 3-(4,5-dimethylthiazol-2-yl)-2,5-diphenyltetrazolium bromide (MTT) and ammonium chloride were obtained from Sigma-Aldrich, France. 5,10,15,20-Tetrakis(4-aminophenyl)porphine was purchased from PorphyrChem, France. Silane-PEG 2000 was obtained from RAPP Polymer, Germany. All chemicals were used as received.

All siRNA used were purchased from Eurogentec (Seraing, Belgium). The Firefly Luciferase siRNA (siFluc) targeting sequence (sense: 5'-CUUACGCUGAGUACUUCGAdTdT-3' and anti-sense: 5'-UCGAAGUACUCAGCGUAAGdTdT-3') and the control siRNA without any biological activity used in two forms as negative control, without any labelling (siCtrl) or labelled with ATTO-488 (siCtrl-ATTO-488) (sense: 5'-CGUACGCGGAAUACUUCGAdTdT-3' and anti-sense: 5'-UCGAAGUAUCCGCGUACGdTdT-3').

### Precursors' synthesis

The syntheses of the precursors methyl-(tris(3-trimethoxysilyl)propyl) ammonium iodide<sup>23, 31-32</sup> and tetrasilylated porphyrin<sup>33</sup> were carried out according to the literature.

### **Periodic mesoporous ionosilica nanoparticles' synthesis**

A mixture of sodium hexadecylsulfate SHS (100 mg, 0.3 mmol), 1,3,5-triethylbenzene (1.5 mL) and deionized water (30 mL) was stirred at 70°C for 8 hours at 750 rpm. Then, a mixture of precursors was prepared in 1-propanol: methyl-(tris(3-trimethoxysilyl)propyl) ammonium iodide (187.3 mg, 0.361 mmol) precursor **1** and the tetrasilylated porphyrin (31.6 mg, 0.019 mmol) precursor **2**. The mixture was added drop by drop during 20 minutes under vigorous stirring. Then, an aqueous solution of non-ionic surfactant triblock copolymer F127 (20 mg) was added to the reaction, followed by 600  $\mu\text{L}$  of ammonia (0.1 M) after 5 minutes. Ten minutes later, an aqueous solution of Silane-PEG 2000 (20 mg) was added. The mixture was stirred at 1250 rpm for 16 hours at 70°C. The reaction was cooled to room temperature, and then the synthesized nanoparticles were collected by centrifugation (20k rpm for 15 minutes) and were washed two times with ethanol before surfactant removal with several washes using an ethanolic ammonium chloride solution (6  $\text{g L}^{-1}$ ).

### **Characterization techniques**

Transmission Electron Microscopy (TEM),  $^{29}\text{Si}$  CP-MAS and  $^{13}\text{C}$  CP-MAS NMR cross-polarization magic angle spinning (CP-MAS) solid-state nuclear magnetic resonance (NMR) spectroscopy, nitrogen sorption and Zeta potential/Dynamic Light Scattering (DLS) measurements were carried out as previously reported.<sup>21, 60-62</sup>

### *Ultraviolet-visible (UV-vis) absorption spectroscopy*

UV-Vis absorption spectra were collected at 25°C on a JASCO V-750 spectrophotometer (France) in 10 mm quartz cells, using an aqueous solution of free-porphyrin at 100 µg mL<sup>-1</sup> and an aqueous suspension of nanoparticles at 200 µg mL<sup>-1</sup>.

### *Fluorescence spectroscopy*

Emission spectra were recorded at 25°C on a fluorescence spectrophotometer (FS920, Edinburgh Instruments) with a 450 W continuous xenon arc lamp using a quartz cuvette with 1.0 cm excitation path length and an aqueous solution of free-porphyrin at 100 µg mL<sup>-1</sup> and an aqueous suspension of nanoparticles at 200 µg mL<sup>-1</sup>. Excitation wavelength was 430 nm.

### **Cell lines**

Human breast cancer cell lines MDA-MB-231 and MDA-MB-231-LUC-RFP were grown in DMEM. Human umbilical vein endothelial cells (HUVECs) were maintained in Endothelial cell Growth Medium 2. Both media were supplemented according to the literature.<sup>63-64</sup> All cells were grown at 37°C in humidified atmosphere with 5% CO<sub>2</sub>.

### **Cytotoxicity assay**

MDA-MB-231 cells and HUVECs were seeded in 96-well plates, in their respective medium, at a density of 2000 cells *per* well (200 µL). After 24 hours, cells were incubated with increasing concentrations of nanoparticles ranging from 1 to 100 µg mL<sup>-1</sup>. Control wells were treated with the vehicle. Cells were incubated for 3 days, and then assayed for cell viability. Cell survival values were determined by the colorimetric MTT assay. MTT was added in each well at a final

concentration of  $0.5 \text{ mg mL}^{-1}$  for 4 hours at  $37^\circ\text{C}$ . Then medium was aspirated and the formed purple crystals were dissolved with equal volumes of ethanol/DMSO. The optical density was measured using a multiwell plate reader (Multiskan FC, ThermoFisher Scientific, USA) at 540 nm. The mean absorbance of control cells served as the reference for calculating 100% cellular viability.

### **Photodynamic therapy experiment**

MDA-MB-231 cells were seeded in 96-well plates at a density of 3000 cells *per* well and left to grow for 24 hours. Then cells were incubated with 5 and  $10 \text{ }\mu\text{g mL}^{-1}$  nanoparticles for 24 hours. Non-treated cells were considered as a control. After incubation with PMINPs, cells were exposed (or not) to green light irradiation at 545 nm for 15 min duration ( $34 \text{ J cm}^{-2}$ ). The light beam was focused by a microscope objective lens (4x/0.10). Two days later, the phototoxicity effect of nanoparticles was evaluated using MTT assay as previously described. The percentage of cell viability was calculated according to the control not exposed to light (set as 100%).

The same procedure was performed using the blue light at (450 - 490 nm) for 15 min duration ( $8 \text{ J cm}^{-2}$ ).

### **Cellular Reactive Oxygen Species detection and quantification**

MDA-MB-231 cells were seeded in 96-well plate, then left to grow for 24 hours. Cells were incubated with PMINPs at a concentration of  $20 \text{ }\mu\text{g mL}^{-1}$  for 24 hours. After the incubation period, ROS were detected using DCFDA/H<sub>2</sub>DCFDA-Cellular ROS Assay Kit (Abcam, UK). Control (non-treated) cells and nanoparticles treated cells were incubated with  $20 \text{ }\mu\text{M}$  of DCFDA for 45 min at  $37^\circ\text{C}$ , then cells were exposed (or not) to green light beam under the same conditions as

PDT experiment ( $\lambda_{exc}$  545 nm for 15 min / 34 J cm<sup>-2</sup>). After light exposure, cells were washed two times then visualized using Leica DM.IRB fluorescence microscope at 450 - 490 nm, objective 10x.

The same procedure was performed using the blue light at (450 - 490 nm) for 15 min duration (8 J cm<sup>-2</sup>).

The obtained images (n=6 for each condition) were processed for the cell fluorescence intensity quantification using ImageJ software.

### **Photo-degradation of 1,3-diphenylisobenzofuran (DPBF) and spectral detection of singlet oxygen**

For singlet oxygen evaluations using DPBF probe, several ethanolic suspensions of PMINPs (10  $\mu\text{g mL}^{-1}$ ) mixed to DPBF (35  $\mu\text{M}$ ) in a final volume of 200  $\mu\text{L}$  were illuminated at 450 - 490 nm (blue light) or 545 nm (green light) for different light irradiation times ranging from 15 to 900 seconds. The same procedure was repeated using DPBF solutions only. The decomposition of DPBF was then monitored by the absorbance measurements at 410 nm, using NanoDrop ND-1000 Spectrophotometer (Thermo Fischer Scientific, USA). The experiment was performed three times.

### **Agarose gel retardation assay**

In order to determine the siRNA binding ability to PMINPs, gel retardation assay was carried out. A fixed quantity (0.364  $\mu\text{g}$ ) of siCtrl was added to increasing amounts of PMINPs, in a way to have increasing weight ratios (from 1/3 to 1/30). The mixture was prepared in deionized water and incubated at 37°C for 30 min for effective complex formation. After incubation, the siCtrl/PMINPs complex was mixed with xylene cyanol 0.25% then electrophoresed on 2% (w/v)

agarose gel containing GelRed™ Nucleic Acid Gel Stain (Interchim, France), with running buffer Tris-Borate-EDTA (TBE) 0.5X pH 8.2 at 100 V for 30 min. siCtrl bands were visualized and photographed by an ultraviolet transilluminator (Infinity Gel documentation Imaging, Vilber Lourmat, France). The high binding capacity was expressed by a total retardation of siCtrl, as showed by the disappearance of siCtrl bands on the gel.

### **Evaluation of the stability of the siRNA/PMINPs complexes**

In order to evaluate the stability of the siRNA/PMINPs complex, gel retardation assay was performed at different time points. A fixed amount of siCtrl (0.36 µg) was added to a fixed quantity of PMINPs (3.6 µg), in order to have a weight ratio of (1/10). The mixture was prepared in deionized water and incubated at 37°C for 30 min, 1 h, 4 h, 6 h, 18 h and 24 h, and then electrophoresed on 2% (w/v) agarose gel, as previously described.

### **siRNA/PMINPs complex characterization**

Zeta potential and DLS measurements were performed using Zetasizer Nano ZS (Malvern, UK) at 25°C and pH 7, using standard disposable cuvettes. Different weight ratios of siCtrl and PMINPs were prepared in deionized water and incubated for 30 min at 37°C. Three individual measurements were done immediately after siCtrl/PMINPs complex formation.

### **Cellular uptake kinetics of PMINPs and siRNA/PMINPs complexes**

MDA-MB-231 cells were seeded in 96-well plate, then left to grow for 24 hours at 37°C. Cells were treated with PMINPs (14 µg mL<sup>-1</sup>) or with the complex siCtrl-ATTO-488/PMINPs (100 nM / 14 µg mL<sup>-1</sup>) at a weight ratio of 1/10 for different time intervals (1 h, 4 h, 6 h, 18 h and 24 h). The cellular uptake of PMINPs and complexes was monitored by fluorescence intensity

measurements, using CLARIOstar high performance monochromator multimode microplate reader (BMG Labtech, Ortenberg, Germany). At the end of incubation time, total fluorescence was measured, then cells were washed three times with PBS and the remaining fluorescence was recorded. The results are expressed as a ratio of remaining fluorescence and total fluorescence RF/TF (%). Fluorescence intensities were corrected according to the total number of living cells in each well, determined by MTT assay as previously described.

### **Imaging**

MDA-MB-231 cells were seeded into glass bottom 8-well tissue culture chambers (SARSTEDT, Germany), at a density of  $10^6$  cells  $\text{cm}^{-2}$  for 24 hours. Then, cells were incubated for 4 hours with 500  $\mu\text{L}$  culture medium containing complex siCtrl-ATTO-488 (100 nM)/PMINPs ( $14 \mu\text{g mL}^{-1}$ ) using weight ratio 1/10, free-PMINPs, free siCtrl-ATTO-488 (100 nM) and Lipofectamine<sup>TM</sup> RNAiMAX Reagent (Invitrogen, USA)/siCtrl-ATTO-488 as a positive control. Untreated cells were considered as a negative control. Twenty minutes prior the end of incubation, cells were treated with CellMask<sup>TM</sup> Orange plasma membrane stain (Invitrogen, France) and Hoechst 33342 (Invitrogen, USA).<sup>65</sup> Then, cells were washed three times with culture medium before observation with LSM780 confocal microscope (Carl Zeiss, France). Cells were scanned at 800 nm for PMINPs, 488 nm for siCtrl-ATTO-488, 561 nm for CellMask and 760 nm for Hoechst, using a high magnification (63x/1.4 OIL Plan-Apo).

### **Mechanism of the cellular uptake of PMINPs and siRNA/PMINPs complexes**

As endocytosis is greatly temperature dependent, we monitored the cellular uptake of PMINPs and the siRNA/PMINPs complexes in two different temperature conditions: 4°C and 37°C. MDA-MB-231 cells were seeded in two 96-well plates, then left to grow for 24 h at 37°C. The first plate

was treated with PMINPs ( $14 \mu\text{g mL}^{-1}$ ) or with the complex siCtrl-ATTO-488/PMINPs ( $100 \text{ nM} / 14 \mu\text{g mL}^{-1}$ ) for four hours at  $37^\circ\text{C}$ . The second plate was treated in the same way, but using cold medium ( $4^\circ\text{C}$ ), then left at  $4^\circ\text{C}$  for four hours. The cellular uptake of PMINPs and complexes was monitored by fluorescence intensity measurements, using CLARIOstar® as previously described. The results are expressed as a percentage of RF/TF (%) at  $4^\circ\text{C}$  compared to the RF/TF (%) at  $37^\circ\text{C}$  (set as 100%). Fluorescence intensities were corrected according to the total number of living cells in each well, determined by MTT assay as previously described.

### **One-photon induced siFluc delivery and cell luciferase assay**

Twenty four hours prior to transfection, MDA-MB-231-Luc-RFP cells were plated at a density of 3000 cells *per* well, into 96-well white plate, PS, F-bottom,  $\mu\text{CLEAR}^{\text{®}}$  (greiner bio-one, Germany). The siFluc/PMINPs complex was freshly prepared in serum free cell culture medium for 30 min at  $37^\circ\text{C}$  using different concentrations of siFluc (50, 100 and 200 nM) at a weight ratio of 1/10. Then, cells were treated (or not) with siFluc/PMINPs complex for four hours. After that, fetal bovine serum was added in each well to reach a 10% serum. After eight hours of incubation, cells were submitted to light irradiation at 545 nm for 5 min duration ( $11.3 \text{ J cm}^{-2}$ ). The light beam was focused by a microscope objective lens (4x/0.10). After 48 hours of transfection, luciferase activity was evaluated by addition of D-Luciferin (Perkin Elmer, USA) at a final concentration of  $10^{-3} \text{ M}$ . Cell luminescence was measured 10 min after, with a plate reader CLARIOstar®. Lipofectamine™ was used as positive control transfection reagent. Results are expressed as a percentage of luminescence activity of treated cells compared to the control cells (set as 100%). Luciferase activity was corrected according to the total number of living cells in each well, as determined by the MTT assay previously described.

The same procedure was performed using the blue light at (450 - 490 nm) for 5 min duration (2.6 J cm<sup>-2</sup>).

### **Study of photochemical internalization and endosomal escape of the siRNA/PMINPs complex by confocal microscopy**

MDA-MB-231 cells were seeded into glass bottom 96-well plate half area (CORNING, USA), at a density of 10<sup>6</sup> cells cm<sup>-2</sup> for 24 hours. Cells were then incubated with 100 µL culture medium containing complex siCtrl (100 nM)/PMINPs (14 µg mL<sup>-1</sup>) at weight ratio 1/10. Untreated cells were considered as a control. Eight hours later, cells were irradiated or not at 545 nm for 5 min (11.3 J cm<sup>-2</sup>). The light beam was focused by a microscope objective lens (4x/0.10). After irradiation, cells were stained with LysoTracker<sup>®</sup> Green DND-26 (Molecular Probes, USA) at a final concentration of 1 µM for 2 hours and 20 min before the end of incubation they stained with Hoechst 33342 at 10 µg mL<sup>-1</sup>. Thereafter, cells were washed three times with culture medium before observation with LSM780 confocal microscope. Cells were scanned at 800 nm for the siCtrl/PMINPs complex, 488 nm for LysoTracker Green and 760 nm for Hoechst, using a high magnification (63x/1.4 OIL Plan-Apo).

### **Statistical analysis**

Results were presented as mean ± standard deviation (SD) of three independent experiments. Statistical analysis was performed using GraphPad Prism. The comparison between groups was analyzed with Student's t-test. Differences were considered statistically significant when p values were less than 0.05. The level of significance was defined as ns (non-statistically significant), \* statistical significance difference (p<0.05), \*\* (p<0.005), \*\*\* (p<0.0005) and \*\*\*\* (p<0.0001).

## ASSOCIATED CONTENT

### Supporting Information

The Supporting Information is available free of charge at <https://pubs.acs.org/doi/10.1021/acsami.xxxxxxx>.

FT-IR spectra of PEG-silane 2000, unpegylated and pegylated ionosilica nanoparticles.

## AUTHOR INFORMATION

### Corresponding Authors

Dr. Nadir BETTACHE, [nadir.bettache@umontpellier.fr](mailto:nadir.bettache@umontpellier.fr)

Dr. Peter HESEMANN, [peter.hesemann@umontpellier.fr](mailto:peter.hesemann@umontpellier.fr)

## NOTES

The authors declare no competing of financial interest.

## ACKNOWLEDGMENTS

The authors thank the “Algerian Ministry of Higher Education and Scientific Research” for the Ph.D. grant to Braham Mezghrani and the Franco-Algerian steering committee for its support. We acknowledge the imaging facility MRI (Montpellier RIO Imaging) platform, member of the national infrastructure France Bio Imaging supported by the French National Research Agency (ANR-10-INBS-04, “Investments for the future”) for confocal imaging facilities access.

## REFERENCES

- (1) Chen, Y.; Shi, J. Chemistry of Mesoporous Organosilica in Nanotechnology: Molecularly Organic–Inorganic Hybridization into Frameworks. *Adv. Mater.* **2016**, *28* (17), 3235-3272.
- (2) Cheng, Y. Y.; Jiao, X. Y.; Fan, W. P.; Yang, Z.; Wen, Y. Q.; Chen, X. Y. Controllable Synthesis of Versatile Mesoporous Organosilica Nanoparticles as Precision Cancer Theranostics. *Biomaterials* **2020**, *256*, 120191.
- (3) Croissant, J. G.; Cattoen, X.; Man, M. W. C.; Durand, J. O.; Khashab, N. M. Syntheses and Applications of Periodic Mesoporous Organosilica Nanoparticles. *Nanoscale* **2015**, *7* (48), 20318-20334.
- (4) Du, X.; Kleitz, F.; Li, X.; Huang, H.; Zhang, X.; Qiao, S.-Z. Disulfide-Bridged Organosilica Frameworks: Designed, Synthesis, Redox-Triggered Biodegradation, and Nanobiomedical Applications. *Adv. Funct. Mater.* **2018**, *28* (26), 1707325.
- (5) Du, X.; Li, X.; Xiong, L.; Zhang, X.; Kleitz, F.; Qiao, S. Z. Mesoporous Silica Nanoparticles with Organo-Bridged Silsesquioxane Framework as Innovative Platforms for Bioimaging and Therapeutic Agent Delivery. *Biomaterials* **2016**, *91*, 90-127.
- (6) Guimaraes, R. S.; Rodrigues, C. F.; Moreira, A. F.; Correia, I. J. Overview of Stimuli-Responsive Mesoporous Organosilica Nanocarriers for Drug Delivery. *Pharmacol. Res.* **2020**, *155*, 104742.
- (7) Teng, Z.; Li, W.; Tang, Y.; Elzatahry, A.; Lu, G.; Zhao, D. Mesoporous Organosilica Hollow Nanoparticles: Synthesis and Applications. *Adv. Mater.* **2019**, *31* (38), 1707612.
- (8) Yang, B.; Chen, Y.; Shi, J. Reactive Oxygen Species (ROS)-Based Nanomedicine. *Chem. Rev.* **2019**, *119* (8), 4881-4985.
- (9) Chen, J.; Luo, H.; Liu, Y.; Zhang, W.; Li, H.; Luo, T.; Zhang, K.; Zhao, Y.; Liu, J. Oxygen-Self-Produced NanoplatforM for Relieving Hypoxia and Breaking Resistance to Sonodynamic Treatment of Pancreatic Cancer. *ACS Nano* **2017**, *11* (12), 12849-12862.
- (10) Li, L.; Yang, Z.; Fan, W.; He, L.; Cui, C.; Zou, J.; Tang, W.; Jacobson, O.; Wang, Z.; Niu, G.; Hu, S.; Chen, X. In Situ Polymerized Hollow Mesoporous Organosilica Biocatalysis Nanoreactor for Enhancing ROS-Mediated Anticancer Therapy. *Adv. Funct. Mater.* **2020**, *30* (4), 1907716.
- (11) Liu, W.; Tian, Y.; Zhang, Y.; Liu, K.; Zhao, S.; Zhang, J.; Su, Y.; Zhao, Y.; Tang, Y.; Sun, J.; Tian, W.; Song, L.; Teng, Z.; Wang, S.; Lu, G. Timely Coordinated Phototherapy Mediated by Mesoporous Organosilica Coated Triangular Gold Nanoprisms. *J. Mater. Chem. B* **2018**, *6* (23), 3865-3875.
- (12) Yang, Z.; Fan, W.; Zou, J.; Tang, W.; Li, L.; He, L.; Shen, Z.; Wang, Z.; Jacobson, O.; Aronova, M. A.; Rong, P.; Song, J.; Wang, W.; Chen, X. Precision Cancer Theranostic Platform by In Situ Polymerization in Perylene Diimide-Hybridized Hollow Mesoporous Organosilica Nanoparticles. *J. Am. Chem. Soc.* **2019**, *141* (37), 14687-14698.
- (13) Yang, Z.; Wen, J.; Wang, Q.; Li, Y.; Zhao, Y.; Tian, Y.; Wang, X.; Cao, X.; Zhang, Y.; Lu, G.; Teng, Z.; Zhang, L. Sensitive, Real-Time, and In-Vivo Oxygen Monitoring for Photodynamic Therapy by Multifunctional Mesoporous Nanosensors. *ACS Appl. Mater. Interf.* **2019**, *11* (1), 187-194.
- (14) Aggad, D.; Jimenez, C. M.; Dib, S.; Croissant, J. G.; Lichon, L.; Laurencin, D.; Richeter, S.; Maynadier, M.; Alsaïari, S. K.; Boufatit, M.; Raehm, L.; Garcia, M.; Khashab, N. M.; Gary-Bobo, M.; Durand, J.-O. Gemcitabine Delivery and Photodynamic Therapy in Cancer Cells via

Porphyrin-Ethylene-Based Periodic Mesoporous Organosilica Nanoparticles. *ChemNanoMat* **2018**, *4* (1), 46-51.

(15) Croissant, J. G.; Picard, S.; Aggad, D.; Klausen, M.; Mauriello Jimenez, C.; Maynadier, M.; Mongin, O.; Clermont, G.; Genin, E.; Cattoën, X.; Wong Chi Man, M.; Raehm, L.; Garcia, M.; Gary-Bobo, M.; Blanchard-Desce, M.; Durand, J.-O. Fluorescent Periodic Mesoporous Organosilica Nanoparticles Dual-Functionalized via Click Chemistry for Two-Photon Photodynamic Therapy in Cells. *J. Mater. Chem. B* **2016**, *4* (33), 5567-5574.

(16) Daurat, M.; Nguyen, C.; Dominguez Gil, S.; Sol, V.; Chaleix, V.; Charnay, C.; Raehm, L.; El Cheikh, K.; Morère, A.; Bernasconi, M.; Timpanaro, A.; Garcia, M.; Cunin, F.; Roessler, J.; Durand, J. O.; Gary-Bobo, M. The Mannose 6-Phosphate Receptor Targeted with Porphyrin-Based Periodic Mesoporous Organosilica Nanoparticles for Rhabdomyosarcoma Theranostics. *Biomater. Sci.* **2020**, *8* (13), 3678-3684.

(17) Jimenez, C. M.; Knezevic, N. Z.; Rubio, Y. G.; Szunerits, S.; Boukherroub, R.; Teodorescu, F.; Croissant, J. G.; Hocine, O.; Seric, M.; Raehm, L.; Stojanovic, V.; Aggad, D.; Maynadier, M.; Garcia, M.; Gary-Bobo, M.; Durand, J.-O. Nanodiamond-PMO for Two-Photon PDT and Drug Delivery. *J. Mater. Chem. B* **2016**, *4* (35), 5803-5808.

(18) Ekiner, G.; Nguyen, C.; Bayır, S.; Dominguez Gil, S.; İsci, Ü.; Daurat, M.; Godefroy, A.; Raehm, L.; Charnay, C.; Oliviero, E.; Ahsen, V.; Gary-Bobo, M.; Durand, J.-O.; Dumoulin, F. Phthalocyanine-Based Mesoporous Organosilica Nanoparticles: NIR Photodynamic Efficiency and siRNA Photochemical Internalization. *Chem. Commun.* **2019**, *55* (77), 11619-11622.

(19) Mauriello Jimenez, C.; Aggad, D.; Croissant, J. G.; Tresfield, K.; Laurencin, D.; Berthomieu, D.; Cubedo, N.; Rossel, M.; Alsaiari, S.; Anjum, D. H.; Sougrat, R.; Roldan-Gutierrez, M. A.; Richeter, S.; Oliviero, E.; Raehm, L.; Charnay, C.; Cattoën, X.; Clément, S.; Wong Chi Man, M.; Maynadier, M.; Chaleix, V.; Sol, V.; Garcia, M.; Gary-Bobo, M.; Khashab, N. M.; Bettache, N.; Durand, J.-O. Porous Porphyrin-Based Organosilica Nanoparticles for NIR Two-Photon Photodynamic Therapy and Gene Delivery in Zebrafish. *Adv. Funct. Mater.* **2018**, *28* (21), 1800235.

(20) Thach, U. D.; Trens, P.; Prelot, B.; Zajac, J.; Hesemann, P. Tuning the Interfacial Properties of Mesoporous Ionosilicas: Effect of Cationic Precursor and Counter Anion. *J. Phys. Chem. C* **2016**, *120* (48), 27412-27421.

(21) Bouchal, R.; Daurat, M.; Gary-Bobo, M.; Da Silva, A.; Lesaffre, L.; Aggad, D.; Godefroy, A.; Dieudonné, P.; Charnay, C.; Durand, J.-O.; Hesemann, P. Biocompatible Periodic Mesoporous Ionosilica Nanoparticles with Ammonium Walls: Application to Drug Delivery. *ACS Appl. Mater. Interf.* **2017**, *9* (37), 32018-32025.

(22) Daurat, M.; Rahmani, S.; Bouchal, R.; Akrouf, A.; Budimir, J.; Nguyen, C.; Charnay, C.; Guari, Y.; Richeter, S.; Raehm, L.; Bettache, N.; Gary-Bobo, M.; Durand, J.-O.; Hesemann, P. Organosilica Nanoparticles for Gemcitabine Monophosphate Delivery in Cancer Cells. *ChemNanoMat* **2019**, *5* (7), 888-896.

(23) Thach, U. D.; Prelot, B.; Pellet-Rostaing, S.; Zajac, J.; Hesemann, P. Surface Properties and Chemical Constitution as Crucial Parameters for the Sorption Properties of Ionosilicas: The Case of Chromate Adsorption. *ACS Appl. Nano Mater.* **2018**, *1* (5), 2076-2087.

(24) Bono, N.; Ponti, F.; Mantovani, D.; Candiani, G. Non-Viral in Vitro Gene Delivery: It is Now Time to Set the Bar! *Pharmaceutics* **2020**, *12* (2).

(25) Patil, S.; Gao, Y. G.; Lin, X.; Li, Y.; Dang, K.; Tian, Y.; Zhang, W. J.; Jiang, S. F.; Qadir, A.; Qian, A. R. The Development of Functional Non-Viral Vectors for Gene Delivery. *Int. J. Mol. Sci.* **2019**, *20* (21).

- (26) Akki, R. A Review Article on Gene Therapy. *J. Drug Deliv. Ther.* **2019**, *9* (4), 688-692.
- (27) Wojnilowicz, M.; Glab, A.; Bertucci, A.; Caruso, F.; Cavalieri, F. Super-resolution Imaging of Proton Sponge-Triggered Rupture of Endosomes and Cytosolic Release of Small Interfering RNA. *ACS Nano* **2019**, *13* (1), 187-202.
- (28) Hoffmann, M.; Hersch, N.; Merkel, R.; Csiszar, A.; Hoffmann, B. Changing the Way of Entrance: Highly Efficient Transfer of mRNA and siRNA via Fusogenic Nano-Carriers. *J. Biomed. Nanotechnol.* **2019**, *15* (1), 170-183.
- (29) Bøe, S. L.; Hovig, E. Enhancing Nucleic Acid Delivery by Photochemical Internalization. *Ther. Deliv.* **2013**, *4* (9), 1125-40.
- (30) Berg, K.; Selbo, P. K.; Prasmickaite, L.; Tjelle, T. E.; Sandvig, K.; Moan, J.; Gaudernack, G.; Fodstad, O.; Kjølrsrud, S.; Anholt, H.; Rodal, G. H.; Rodal, S. K.; Høgset, A. Photochemical Internalization: a Novel Technology for Delivery of Macromolecules into Cytosol. *Cancer Res.* **1999**, *59* (6), 1180-3.
- (31) El Hankari, S.; Motos-Perez, B.; Hesemann, P.; Bouhaouss, A.; Moreau, J. J. E. Pore Size Control and Organocatalytic Properties of Nanostructured Silica Hybrid Materials Containing Amino and Ammonium Groups. *J. Mater. Chem.* **2011**, *21* (19), 6948-6955.
- (32) Nguyen, T. P.; Hesemann, P.; Linh Tran, T. M.; Moreau, J. J. E. Nanostructured Polysilsesquioxanes Bearing Amine and Ammonium Groups by Micelle Templating using Anionic Surfactants. *J. Mater. Chem.* **2010**, *20* (19), 3910-3917.
- (33) Lerouge, F.; Cerveau, G.; Corriu, R. J. P.; Stern, C.; Guillard, R. Self-Organization of Porphyrin Units Induced by Magnetic Field during Sol-Gel Polymerization. *Chem. Commun.* **2007**, (15), 1553-1555.
- (34) Talamini, L.; Picchetti, P.; Ferreira, L. M.; Sitia, G.; Russo, L.; Violatto, M. B.; Travaglini, L.; Fernandez Alarcon, J.; Righelli, L.; Bigini, P.; De Cola, L. Organosilica Cages Target Hepatic Sinusoidal Endothelial Cells Avoiding Macrophage Filtering. *ACS Nano* **2021**.
- (35) Aggarwal, P.; Hall, J. B.; McLeland, C. B.; Dobrovolskaia, M. A.; McNeil, S. E. Nanoparticle Interaction with Plasma Proteins as it relates to Particle Biodistribution, Biocompatibility and Therapeutic Efficacy. *Adv. Drug Deliver. Rev.* **2009**, *61* (6), 428-437.
- (36) Mahmoudi, M.; Lynch, I.; Ejtehadi, M. R.; Monopoli, M. P.; Bombelli, F. B.; Laurent, S. Protein-Nanoparticle Interactions: Opportunities and Challenges. *Chem. Rev.* **2011**, *111* (9), 5610-5637.
- (37) Llewellyn, P. 13 - Adsorption by Ordered Mesoporous Materials. In *Adsorption by Powders and Porous Solids (Second Edition)*; Rouquerol, F.; Rouquerol, J.; Sing, K. S. W.; Llewellyn, P.; Maurin, G., Eds.; Academic Press: Oxford, 2014; pp 529-564.
- (38) Laurencin, D.; Yot, P. G.; Gervais, C.; Guari, Y.; Clement, S.; Elkaim, E.; Paillet, M.; Cot, D.; Richeter, S. Synthesis, Characterization and Modeling of Self-Assembled Porphyrin Nanorods. *J. Porphyr. Phthalocya.* **2019**, *23* (11-12), 1346-1354.
- (39) Fagadar-Cosma, E.; Enache, C.; Vlascici, D.; Fagadar-Cosma, G.; Stadler, H.; Bazylak, G. Nanostructured Glasses Based on Hybrid Silica Materials Incorporating a New Asymmetrical Phenyl-Substituted Porphyrin. *Open Chem. Biomed Methods J.* **2009**, *2*, 99-106.
- (40) Chen, X.; Zhong, Z.; Xu, Z.; Chen, L.; Wang, Y. 2',7'-Dichlorodihydrofluorescein as a Fluorescent Probe for Reactive Oxygen Species Measurement: Forty Years of Application and Controversy. *Free Radical Res.* **2010**, *44* (6), 587-604.
- (41) Wang, H.; Yang, X.; Shao, W.; Chen, S.; Xie, J.; Zhang, X.; Wang, J.; Xie, Y. Ultrathin Black Phosphorus Nanosheets for Efficient Singlet Oxygen Generation. *J. Am. Chem. Soc.* **2015**, *137* (35), 11376-11382.

- (42) Espinoza, C.; Trigos, Á.; Medina, M. E. Theoretical Study on the Photosensitizer Mechanism of Phenalenone in Aqueous and Lipid Media. *J. Phys. Chem. A* **2016**, *120* (31), 6103-6110.
- (43) Fan, W.; Huang, P.; Chen, X. Overcoming the Achilles' Heel of Photodynamic Therapy. *Chem. Soc. Rev.* **2016**, *45* (23), 6488-6519.
- (44) Park, J.; Jiang, Q.; Feng, D. W.; Mao, L. Q.; Zhou, H. C. Size-Controlled Synthesis of Porphyrinic Metal-Organic Framework and Functionalization for Targeted Photodynamic Therapy. *J. Am. Chem. Soc.* **2016**, *138* (10), 3518-3525.
- (45) Liang, X. L.; Chen, M.; Bhattarai, P.; Hameed, S.; Dai, Z. F. Perfluorocarbon@Porphyrin Nanoparticles for Tumor Hypoxia Relief to Enhance Photodynamic Therapy against Liver Metastasis of Colon Cancer. *ACS Nano* **2020**, *14* (10), 13569-13583.
- (46) Sun, Y.; Chen, Z. L.; Yang, X. X.; Huang, P.; Zhou, X. P.; Du, X. X. Magnetic Chitosan Nanoparticles as a Drug Delivery System for Targeting Photodynamic Therapy. *Nanotechnology* **2009**, *20* (13).
- (47) Dib, S.; Aggad, D.; Jimenez, C. M.; Lakrafi, A.; Hery, G.; Nguyen, C.; Durand, D.; Morere, A.; El Cheikh, K.; Sol, V.; Chaleix, V.; Gil, S. D.; Bouchmella, K.; Raehm, L.; Durand, J. O.; Boufatit, M.; Cattoen, X.; Man, M. W. C.; Bettache, N.; Gary-Bobo, M. Porphyrin-based Bridged Silsesquioxane Nanoparticles for Targeted Two-Photon Photodynamic Therapy of Zebrafish Xenografted with Human Tumor. *Cancer Rep.* **2019**, *2* (5).
- (48) Tu, H. L.; Lin, Y. S.; Lin, H. Y.; Hung, Y.; Lo, L. W.; Chen, Y. F.; Mou, C. Y. In Vitro Studies of Functionalized Mesoporous Silica Nanoparticles for Photodynamic Therapy. *Adv. Mater.* **2009**, *21* (2), 172-+.
- (49) Qian, J.; Gharibi, A.; He, S. L. Colloidal Mesoporous Silica Nanoparticles with Protoporphyrin IX encapsulated for Photodynamic Therapy. *J. Biomed. Opt.* **2009**, *14* (1).
- (50) Liang, X. Y.; Xie, Y. H.; Wu, J. X.; Wang, J.; Petkovic, M.; Stepic, M.; Zhao, J. Z.; Ma, J.; Mi, L. Functional Titanium Dioxide Nanoparticle Conjugated with Phthalocyanine and Folic Acid as a promising Photosensitizer for Targeted Photodynamic Therapy In Vitro and In Vivo. *J. Photoch. Photobio. B* **2021**, *215*.
- (51) Zhao, B. Z.; Yin, J. J.; Bilski, P. J.; Chignell, C. F.; Roberts, J. E.; He, Y. Y. Enhanced Photodynamic Efficacy towards Melanoma Cells by Encapsulation of Pc4 in Silica Nanoparticles. *Toxicol. Appl. Pharm.* **2009**, *241* (2), 163-172.
- (52) Huang, P.; Li, Z. M.; Lin, J.; Yang, D. P.; Gao, G.; Xu, C.; Bao, L.; Zhang, C. L.; Wang, K.; Song, H.; Hu, H. Y.; Cui, D. X. Photosensitizer-Conjugated Magnetic Nanoparticles for In Vivo Simultaneous Magnetofluorescent Imaging and Targeting Therapy. *Biomaterials* **2011**, *32* (13), 3447-3458.
- (53) Huang, P.; Xu, C.; Lin, J.; Wang, C.; Wang, X. S.; Zhang, C. L.; Zhou, X. J.; Guo, S. W.; Cui, D. X. Folic Acid-conjugated Graphene Oxide Loaded with Photosensitizers for Targeting Photodynamic Therapy. *Theranostics* **2011**, *1*, 240-250.
- (54) Kim, J.; Cho, H. R.; Jeon, H.; Kim, D.; Song, C.; Lee, N.; Choi, S. H.; Hyeon, T. Continuous O-2-Evolving MnFe<sub>2</sub>O<sub>4</sub> Nanoparticle-Anchored Mesoporous Silica Nanoparticles for Efficient Photodynamic Therapy in Hypoxic Cancer. *J. Am. Chem. Soc.* **2017**, *139* (32), 10992-10995.
- (55) Li, J. Y.; Guo, D. D.; Wang, X. M.; Wang, H. P.; Jiang, H.; Chen, B. A. The Photodynamic Effect of Different Size ZnO Nanoparticles on Cancer Cell Proliferation In Vitro. *Nanoscale Res. Lett.* **2010**, *5* (6), 1063-1071.
- (56) Mao, S.; Germershaus, O.; Fischer, D.; Linn, T.; Schnepf, R.; Kissel, T. Uptake and Transport of PEG-graft-Trimethyl-Chitosan Copolymer-Insulin Nanocomplexes by Epithelial Cells. *Pharm. Res.* **2005**, *22* (12), 2058-2068.

- (57) Chang, C. C.; Wu, M.; Yuan, F. Role of Specific Endocytic Pathways in Electrotransfection of Cells. *Mol. Ther. Methods Clin. Dev.* **2014**, *1*.
- (58) Kanasty, R. L.; Whitehead, K. A.; Vegas, A. J.; Anderson, D. G. Action and Reaction: the Biological Response to siRNA and its Delivery Vehicles. *Mol. Ther.* **2012**, *20* (3), 513-24.
- (59) Selbo, P. K.; Weyergang, A.; Høgset, A.; Norum, O. J.; Berstad, M. B.; Vikdal, M.; Berg, K. Photochemical Internalization provides Time- and Space-Controlled Endolysosomal Escape of Therapeutic Molecules. *J. Control. Release* **2010**, *148* (1), 2-12.
- (60) Bouchal, R.; Miletto, I.; Thach, U. D.; Prelot, B.; Berlier, G.; Hesemann, P. Ionosilicas as efficient adsorbents for the separation of diclofenac and sulindac from aqueous media. *New J. Chem.* **2016**, *40* (9), 7620-7626.
- (61) Thach, U. D.; Hesemann, P.; Yang, G. Z.; Geneste, A.; Le Caer, S.; Prelot, B. Ionosilicas as efficient sorbents for anionic contaminants: Radiolytic stability and ion capacity. *J. Colloid Interf. Sci.* **2016**, *482*, 233-239.
- (62) Thach, U. D.; Prelot, B.; Hesemann, P. Design of ionosilicas: Tailoring ionosilicas for the efficient adsorption of p-aminosalicylate. *Sep. Purif. Technol.* **2018**, *196*, 217-223.
- (63) Ali, L. M. A.; Mathlouthi, E.; Cahu, M.; Sene, S.; Daurat, M.; Long, J.; Guari, Y.; Salles, F.; Chopineau, J.; Devoisselle, J. M.; Larionova, J.; Gary-Bobo, M. Synergic effect of doxorubicin release and two-photon irradiation of Mn<sup>2+</sup>-doped Prussian blue nanoparticles on cancer therapy. *RSC Adv.* **2020**, *10* (5), 2646-2649.
- (64) Seisenbaeva, G. A.; Ali, L. M. A.; Vardanyan, A.; Gary-Bobo, M.; Budnyak, T. M.; Kessler, V. G.; Durand, J. O. Mesoporous silica adsorbents modified with amino polycarboxylate ligands-functional characteristics, health and environmental effects. *J. Hazard. Mater.* **2021**, *406*, 16.
- (65) Ali, L. M. A.; Simon, M.; El Cheikh, K.; Aguesseau-Kondrotas, J.; Godefroy, A.; Nguyen, C.; Garcia, M.; Morere, A.; Gary-Bobo, M.; Maillard, L. Topological Requirements for CI-M6PR-Mediated Cell Uptake. *Bioconjugate Chem.* **2019**, *30* (10), 2533-2538.